

Copyright © 2000, by the author(s).
All rights reserved.

Permission to make digital or hard copies of all or part of this work for personal or classroom use is granted without fee provided that copies are not made or distributed for profit or commercial advantage and that copies bear this notice and the full citation on the first page. To copy otherwise, to republish, to post on servers or to redistribute to lists, requires prior specific permission.

**SPATIALLY RESOLVED OPTICAL
EMISSION SPECTROSCOPY
FOR PLASMA ETCHING**

by

Jae-Wook Lee

Memorandum No. UCB/ERL M00/49

29 September 2000

**SPATIALLY RESOLVED OPTICAL
EMISSION SPECTROSCOPY
FOR PLASMA ETCHING**

by

Jae-Wook Lee

Memorandum No. UCB/ERL M00/49

29 September 2000

ELECTRONICS RESEARCH LABORATORY

College of Engineering
University of California, Berkeley
94720

Spatially Resolved Optical Emission Spectroscopy for Plasma Etching

Jae-Wook Lee

Research Project

Submitted to the Department of Electrical Engineering and Computer Sciences,
University of California at Berkeley, in partial satisfaction of the requirements for the
degree of **Master of Science, Plan II.**

Approval for the Report and Comprehensive Examination:

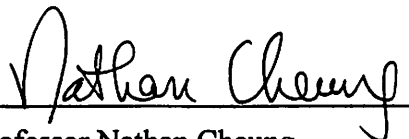
Committee:



Professor Costas J. Spanos
Research Advisor

9/20/2000

(Date)



Professor Nathan Cheung
Second Reader

9/29/2000

| | |
|-------------------------------------------------------------------------|-----------|
| CHAPTER 1 | 2 |
| INTRODUCTION: SPATIALLY RESOLVED OPTICAL EMISSION SPECTROSCOPY 2 | |
| 1.1 MOTIVATION | 2 |
| 1.2 BACKGROUND | 3 |
| CHAPTER 2 | 9 |
| SROES SETUP | 9 |
| CHAPTER 3 | 12 |
| RESULTS AND ANALYSIS I | 12 |
| CHAPTER 4 | 37 |
| INTRODUCTION: TOMOGRAPHY..... | 37 |
| 4.1 MOTIVATION | 37 |
| 4.2 TOMOGRAPHY APPLICATIONS | 37 |
| CHAPTER 5 | 42 |
| TOMOGRAPHY SIMULATION..... | 42 |
| 5.1 GENERAL TOMOGRAPHIC IDEA | 42 |
| 5.2 COMPUTER SIMULATION | 44 |
| 5.3 OPTICAL BENCH TESTING | 49 |
| CHAPTER 6 | 53 |
| TOMOGRAPHY SETUP | 53 |
| CHAPTER 7 | 57 |
| RESULTS AND ANALYSIS II..... | 57 |
| REFERENCES | 69 |

Chapter 1

Introduction: Spatially Resolved Optical Emission Spectroscopy

1.1 Motivation

As the semiconductor industry pushes critical dimensions below $0.10\ \mu\text{m}$, process variability requirements in semiconductor manufacturing become more stringent. Also, as the industry moves toward 300 mm wafer production, wafer uniformity issues are becoming more important and need to be addressed frequently. Due to the sequential nature of the semiconductor processing, any one processing step can possibly contribute to poor yield and/or degraded device performance, resulting in millions of dollars wasted in processing time, equipment usage, and lost revenue. One of the main contributors to this non-uniformity is plasma etching.

Plasma etching has two different etching modes: timed etching and plasma emission sensor triggered etching. Timed etching is done in a situation where relevant plasma emission signals are too weak to trigger proper sensor readings. Emission sensor triggered etching is done when relevant plasma emission signals are strong enough to be detected by an end-point sensor. The former is typically done when the total etched area of a wafer is too small to give rise to a significant amount of plasma emission, when the desired layer(s) is etched through. Such a case may be a contact-hole etching. The latter is done when etching produces detectable signals when the desired layer(s) is etched

through. This type of etching may be a polysilicon gate definition, metal line etching, and contact hole etching with intentionally added etching area for producing a strong enough signal. This report is concerned with the emission sensor-based etching.

1.2 Background

In a typical commercial plasma etcher, a single or a dual wavelength detector is installed on the view-port of an etcher, for end-point detection. These kinds of detectors are monitoring specific wavelengths that are characteristic of a given etching recipe, collecting signals over the entire wafer. This detection scheme remains unchanged essentially for several years. The only changes are in how the plasma emission signals are processed. Specifically, a dedicated module approach is used for end-point detectors nowadays, where a dedicated Pentium class computer does extensive end-point signal processing, as opposed to a simple intensity reading that has been done in previous years.

✓ However, one of the disadvantages of the traditional end-point scheme has been that it provides no spatial end-point information across a wafer. In recent years, addressing the importance of spatial information on within-wafer uniformity improvements, several researchers reported 'spatially resolved optical emission spectroscopy' (SROES) schemes. In 1995, Buie et al. from the University of Michigan tried to rebuild radial emission profiles using Abel inversion [1]. This approach involved the collection of one-dimensional intensity reading at one wavelength, as shown in Figure 1. Each spatially resolved point roughly collected a line integration of plasma intensity above the wafer. Assuming the radial symmetry of the plasma discharge during etching, Abel inversion was performed. This method demonstrated a radial intensity profile

reconstruction technique that could possibly be used to obtain the actual plasma emission profile. However, it suffered from a couple of disadvantages. First, it required a view-port that is wider than the diameter of the wafer, leaving the collected signal susceptible to the lateral transmission variation of the view-port. Second, the relative intensity reading had high uncertainty (15% ~ 20%), and the reconstructed profiles were sensitive to noise [1]. In 1997, S. Shannon et al from the University of Michigan applied a generalized Tkhonov regularization with a rotating sensor stage to generate robust radial emission profiles. Figure 2 illustrates this setup, which could be manually rotated around the plasma chamber at a fine angle (0.2°) and collect emissions from a narrow ($\sim 6^\circ$) wedge. In addition, plasma emissions were collected using a narrower portion of the view-port [2]. Thus, this setup minimized non-uniform intensity contributions from

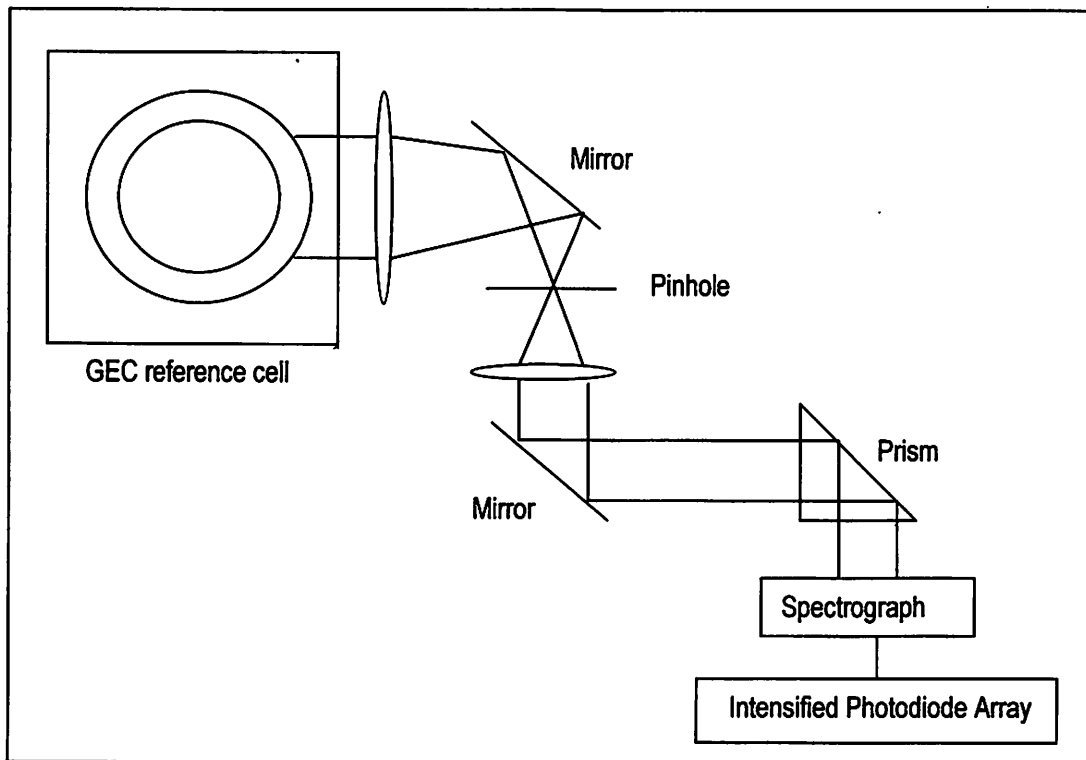


Figure 1. SROES scheme from the University of Michigan in 1995

the films deposited on the view-port. However, the reconstructed emission profiles still suffered from some sensitivity to noise, and a lengthy, sequential scanning was required.

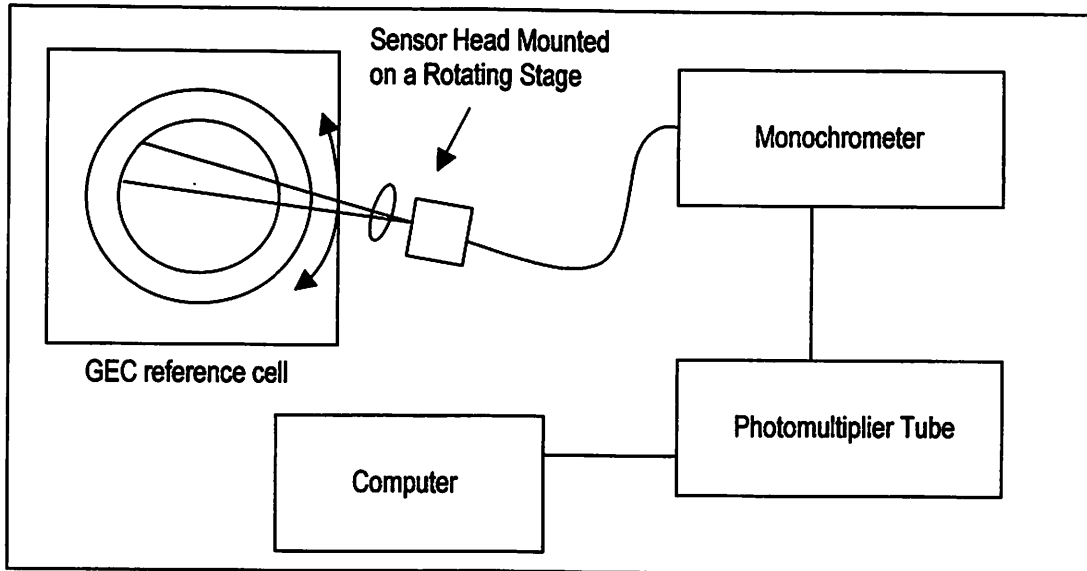


Figure 2. SROES scheme from the University of Michigan in 1997

In 1997, Roawen Chen and Costas Spanos from the University of California at Berkeley used a rotating mirror structure to capture spatially resolved end-point occurrences. In this setup, a stepper motor and a photodiode array in conjunction with a diffraction grating as shown in Figure 3 were used [3]. The setup was similar to that used by S. Shannon, with several differences. First, an externally driven stepper motor was used to speed up the data acquisition. This allowed Chen and Spanos to detect the spatial signature of plasma transitions with 2 ~ 3 second resolution, while the Michigan setup was limited to steady state observations. Second, wavelengths from 200nm to 800nm were monitored. Third, the rotating mirror depicted in Figure 3 was the only moving part during the data acquisition. This setup collected a four-dimensional data set as shown in Figure 4: wavelength, intensity, position, and time. Then, the spectral information was compressed using Principal Component Analysis (PCA). PCA transforms a highly

correlated data set into a set of linearly independent data. Principal component scores at each position, which were obtained using a first few principal components, were used to detect end-point occurrences along angular positions across the wafer.

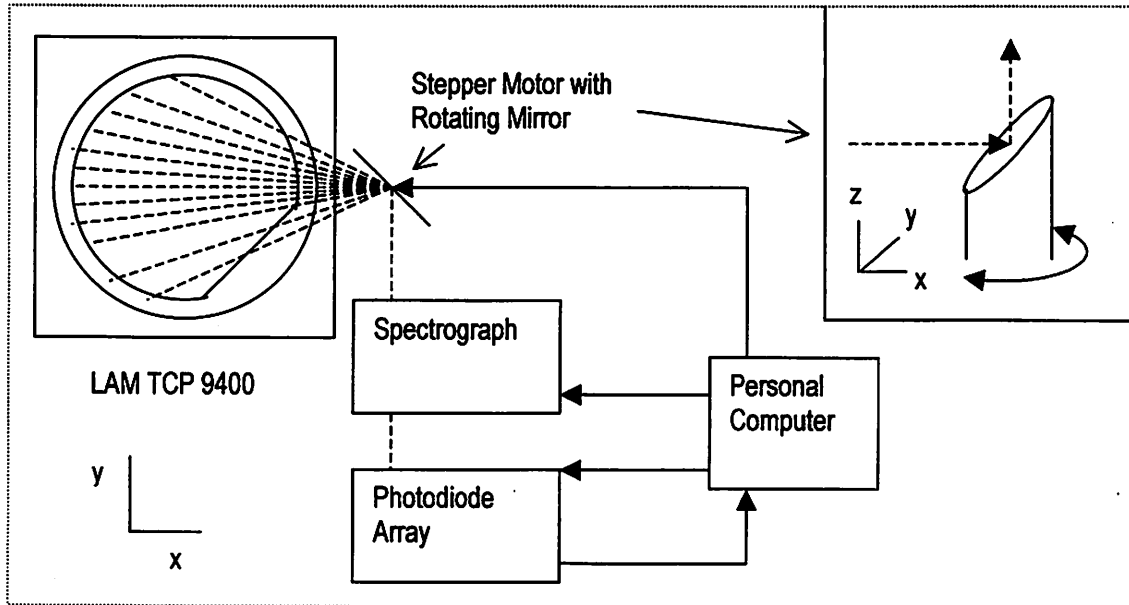


Figure 3. SROES scheme used at UC Berkeley

This data acquisition scheme did not use Abel inversion but used principal component scores to detect end-point occurrences across a wafer as shown in Figure 5. Nevertheless, due to the sequential nature of the data collection and slow data acquisition rate (limited to ~ 2.6 seconds per sweep at 20 angular points, due to the electrical and mechanical limitations of the stepper motor), only rough estimates of end-points were possible as shown in Figure 4 and 6.

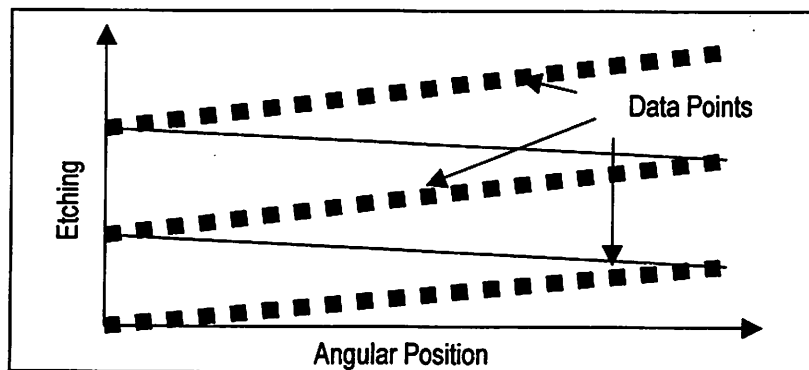


Figure 4. Data collection order of SROES scheme in Figure 3

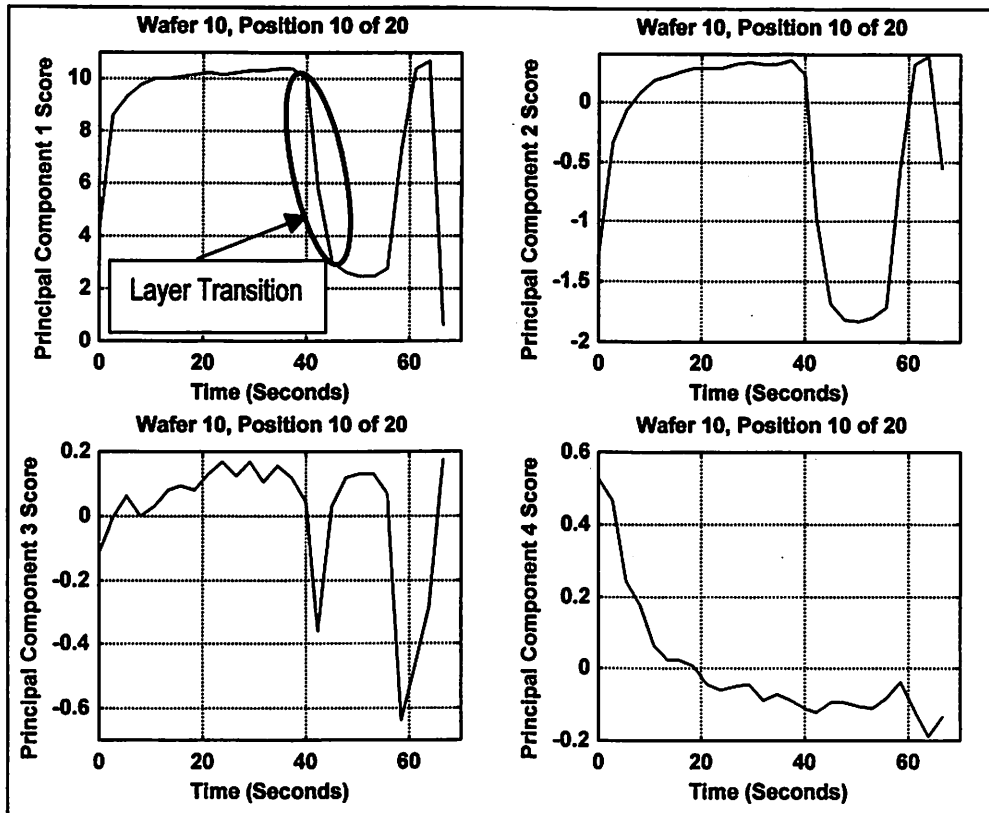


Figure 5. Principal component scores 1-4 of a single wafer at a single position

In this project report, the above limitations are addressed, and an alternate measurement approach is used in order to achieve fast data rate (= 33 ms per data point per wafer position) while maintaining the same amount of spatial resolution (20 angular positions across a wafer). This report contains two experiments. Chapters 1, 2, and 3 contain introduction, experimental setup, and results and analysis of spatially resolved optical emission end-point detection respectively. This experiment deals with one-dimensional spatially resolved views of wafers obtained from one view-port. Thus, this enables a user to detect end-points across a wafer in a lateral direction as shown in Figure 9 and 10. In the second part of the report (chapters 4,5,6, and 7), an extension to the setup described in the first part of the report is introduced. The second experiment explores the

idea of incorporating tomography to the spatially resolved optical emission end-point detection. This scheme generates spatially resolved two-dimensional emission image maps of wafers from a set of one-dimensional views obtained at various angles. Appropriate computer and optical bench simulations are presented followed by wafer run data.

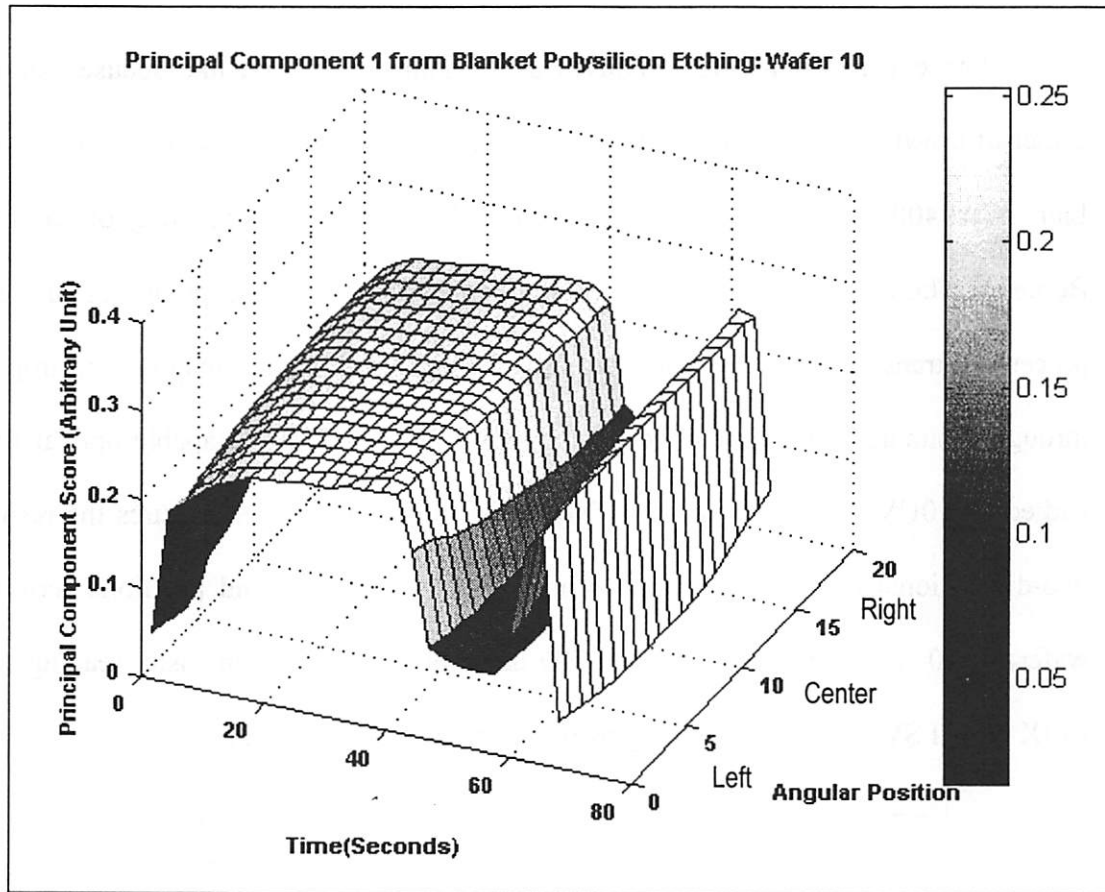


Figure 6. Principal component 1 scores across a single wafer.

Chapter 2

SROES Setup

The experimental setup involves a Newtonian telescope that focuses onto the center of a wafer as shown in Figure 7. The telescope is placed outside the view-port of Lam TCP 9400 polysilicon plasma etcher, in the Microlab at the University of California, Berkeley. The plasma emission focused and gathered by the telescope during an etching process is transmitted to the entrance slit of a Chromex 250IS imaging spectrograph, through a bundle of Polymicro Technology FVP 300330370 UV capable optical fibers. Cidtec I3710UV gated intensified CID (Charge Injection Device) captures the resulting two-dimensional emission intensity information (wavelengths and positions across the wafer) at 30 frames per second. The CID delivers 8 bit analog intensity readings. An EPIX PIXCI SV4 imaging board digitizes and stores the analog data.

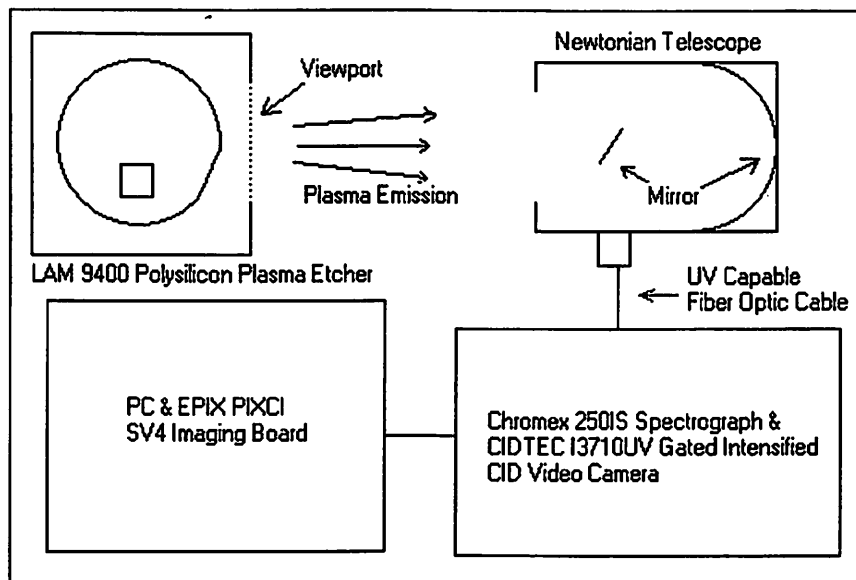


Figure 7. Spatially resolved OES data collection scheme

The Polymicro Technology FVP 300330370 UV fiber optic cable consists of 22 individual fiber strands. Each strand has 300 μm (diameter) silica core, 15 μm (layer thickness) doped silica cladding, and 20 μm (layer thickness) polyimide buffer. Figure 8 shows the schematics of the Chromex plug fixture head and fiber arrangement at each end of the cable. The spacing of the fiber strands at each end of the cable is determined so that plasma emission just above a wafer, roughly 7 cm across, is focused and imaged on the CID chip.

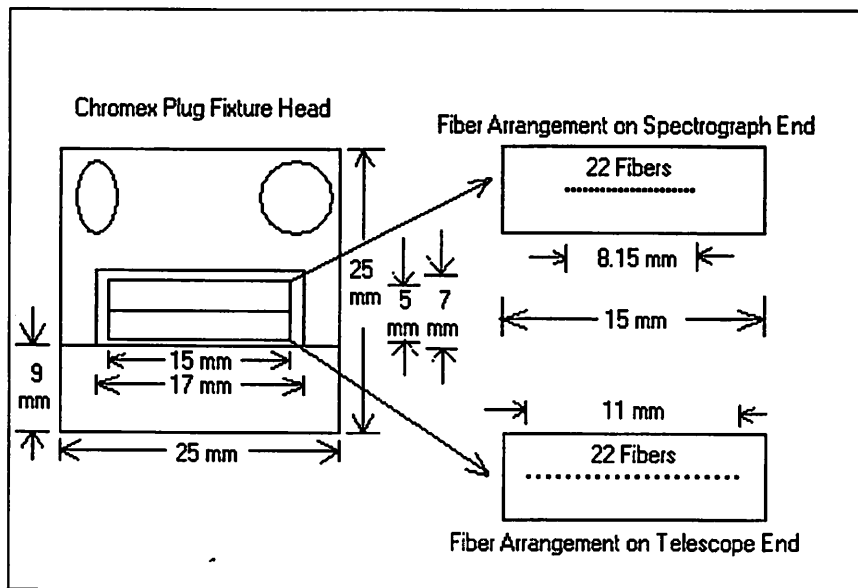


Figure 8. Chromex plug fixture schematics and fiber arrangement

In order to determine the capabilities of the setup, 12 patterned wafers were prepared for etching and signal collection. Figure 9 shows the cross section of a pitted wafer. First, 300 \AA of SiO_2 layer was thermally grown on all 12 test wafers. Then, roughly 5000 \AA of polysilicon layer was deposited using low-pressure chemical vapor deposition (LPCVD) on all 12 wafers. Finally, full-wafer 1:1 contact masks with 1-inch²

and 1cm^2 openings were used to pattern eight wafers according to the arrangement in Table 1. The eight wafers were pre-thinned using Lam TCP 9400. The pit area polysilicon thickness was reduced down to about $1000\text{-}1500\text{ \AA}$. The CMOS59 gate mask at the Microlab was used to pattern all 12 wafers. The mask produced about 90% open area on the wafers. Four baseline wafers (wafers without a pit but only gate patterns) were included to measure the emission transient effect during an active etching. Right-pitted wafers were not prepared. This was because of the wafer clamp bar that comes down and blocks emission from the right-pit during an active etching.

Table 1. Test wafer arrangement

| Pit Size (Area) | Pit position with respect to the view-port | | |
|---------------------------|--------------------------------------------|--------|----------|
| | Left | Center | Baseline |
| Large (1 in^2) | 2 | 2 | |
| Small (1 cm^2) | 2 | 2 | |
| None | | | 4 |

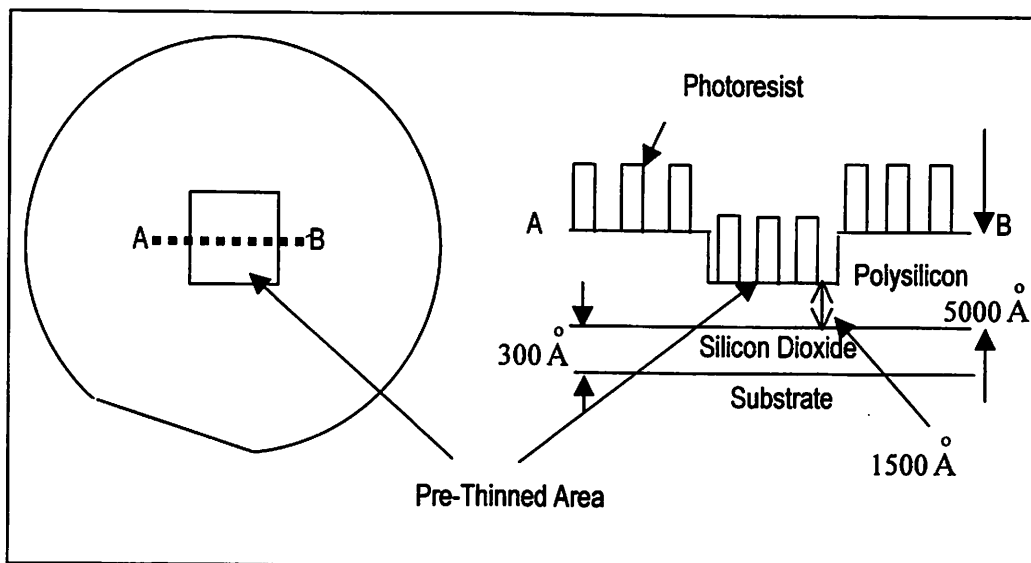


Figure 9. Center-pitted wafer and its cross section.

Chapter 3

Results and Analysis I

The original data for each wafer was an 8-bit TIFF image sequence (674 frames) of 120 (vertical pixels) by 752 (horizontal pixels). The 120 vertical pixels covered roughly 20 fiber strands while 752 horizontal pixels covered wavelengths from 370nm to 440nm. The 120 vertical pixels were grouped into 20 super-pixels, where each super-pixel represented a single fiber strand. This was also done in order to increase the signal to noise ratio of the emission. Figure 10 describes rough positions of the pits and approximate positions of 20 fibers relative to the pits. Figure 11 through 13 show typical emission profiles at different points on a wafer during an etching.

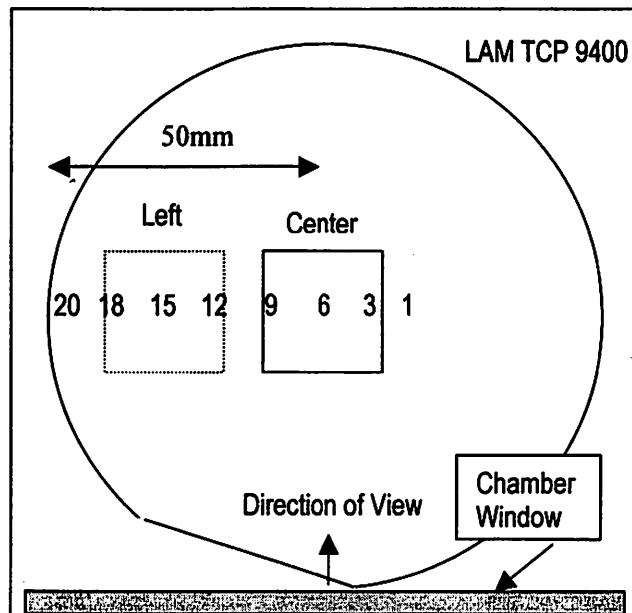


Figure 10. Typical 1 inch pit positions (left and center) and locations of fiber focus (1 through 20)

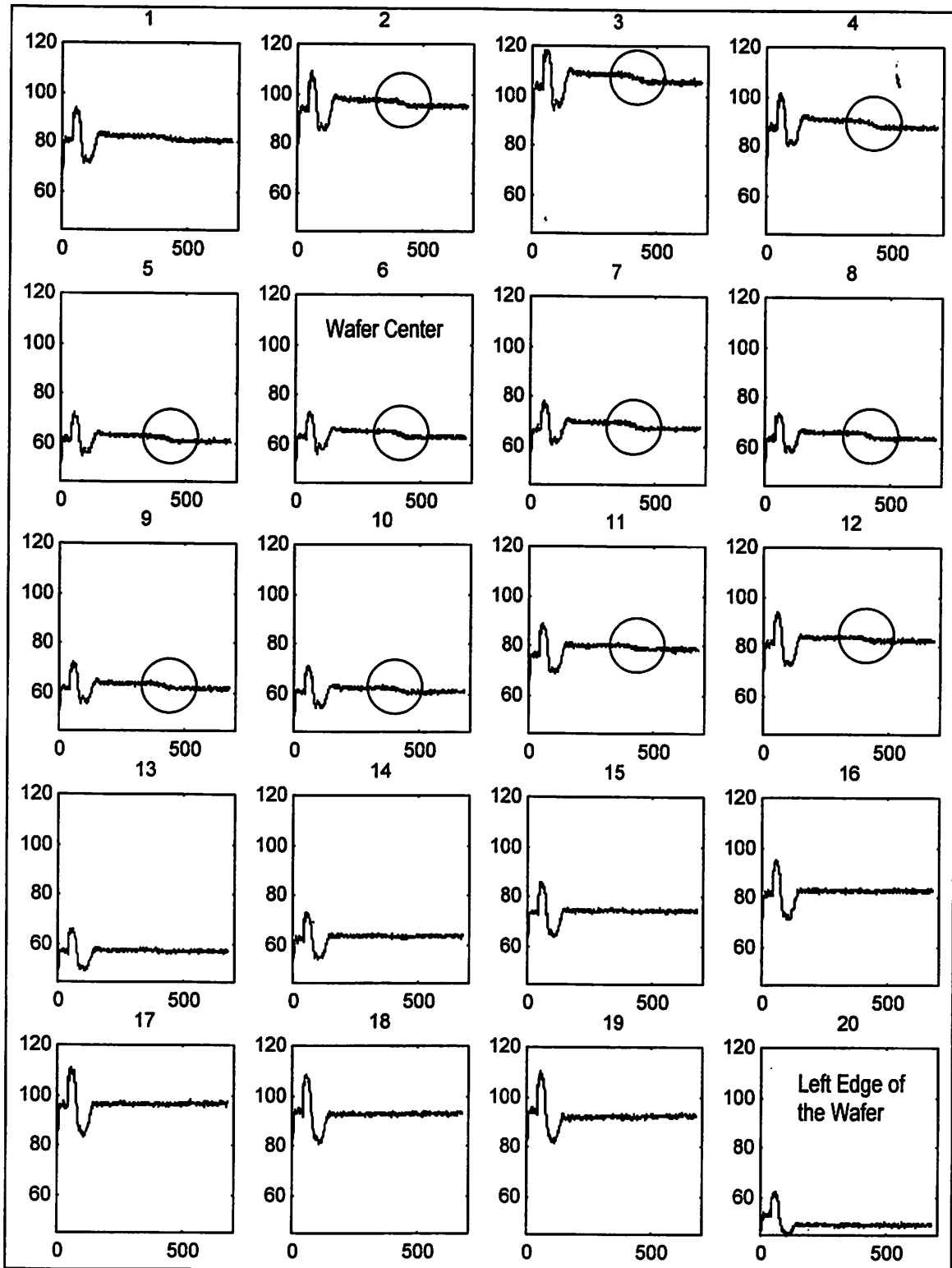


Figure 11. Typical average emission intensity of a 1-inch center-pitted wafer (time frame vs. emission intensity). Circles highlight the signal transition over the pit.

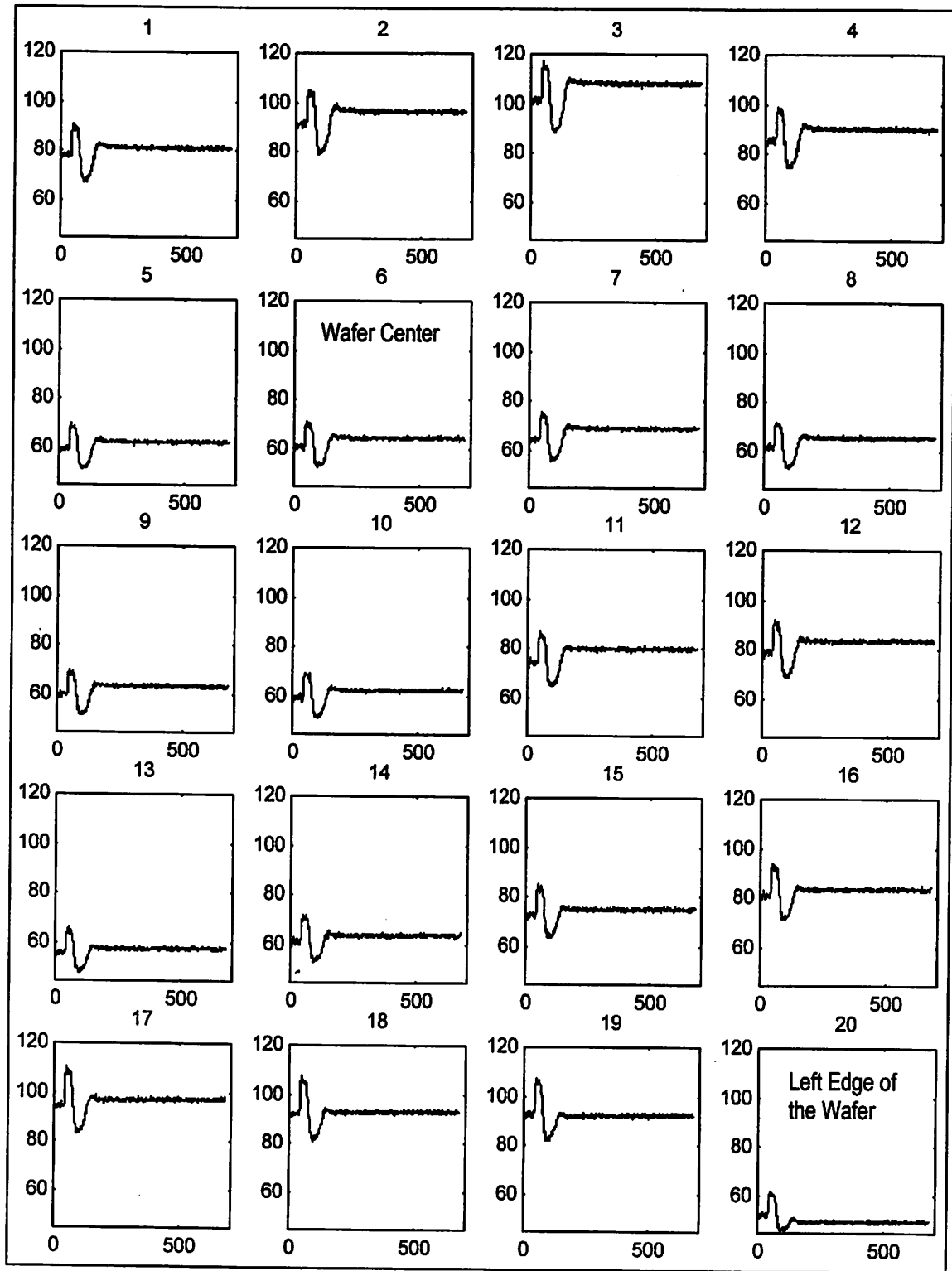


Figure 12. Typical average emission intensity of a baseline wafer without end-points (time frame vs. emission intensity)

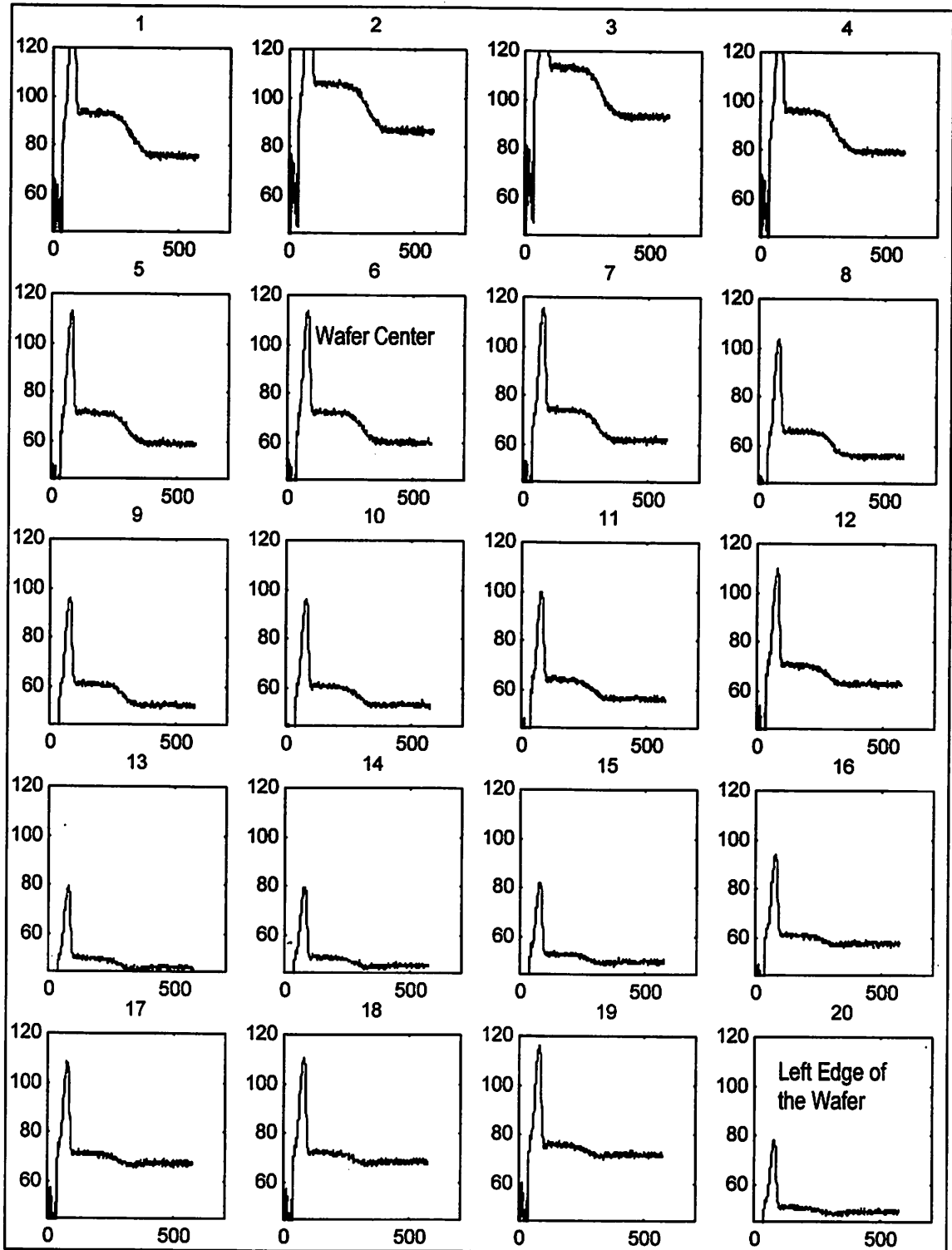


Figure 13. Typical average emission intensity of a baseline wafer with end-points (time frame vs. emission intensity)

Figure 11 shows a typical emission profile of a 1 inch² pitted wafer. The figure shows that after a few seconds of initial fluctuation, the emission intensity relatively flattens out. After a while, end-points occur over the pre-thinned areas. This is recorded as a drop in the signal intensity. This is mainly due to the lack of SiCl₂, which is a main by-product of the Cl₂-based polysilicon etching. Each fiber position roughly covers 0.35cm across a wafer. Therefore, at least seven positions are expected to show some signal decrease during end-point occurrences. Actually, the emission intensity decreases in about 12 different positions around the center of the pit, which is the position 6 in Figure 11. The circles drawn in Figure 11 represent the end-point related signal drops. This is most likely occurring due to SiCl₂ diffusing to the pitted areas, where the by-product concentration is low. Thus, the resulting profile is a rather smooth drop off in the emission intensity as a function of position. This can be seen in Figure 32. Also, due to imperfect alignment of fibers, average emission intensity varies from position to position. Therefore, the emission intensity has been normalized to the pre-end-point signal level in order to produce Figure 32.

Figure 12 shows a typical emission profile of a baseline wafer etching. The wafers used contain gate patterns but do not have any pre-thinned areas. As in Figure 11, there is an initial signal fluctuation. As mentioned in chapter 2, baseline wafers are included in the experiment in order to counteract any gradual signal changes that may occur during an etching. However, the emission intensity is relatively flat during the etching without any apparent intensity drift. Therefore, baseline wafer data are not used in data analysis.

Figure 13 shows a typical emission profile of a blanket wafer etching. The wafers used did not have any pre-thinned areas or gate patterns. The entire polysilicon layer was etched away. This resulted in strong transition signals across the wafer.

Figures 14, 15, and 16 compare the average signal intensity as a function of time at different points on a wafer: above the pit and outside the pit. As the figures show, quite distinct signal transitions are observable above the pit areas for 1inch^2 pits. On the other hand, it is very difficult to find an appreciable and consistent amount of transition signals from 1cm^2 pits. Actually, the contour plots in Figures 31 and 33 show some trace of the pits. However, the noisy signals are not quite suitable for end-point detection.

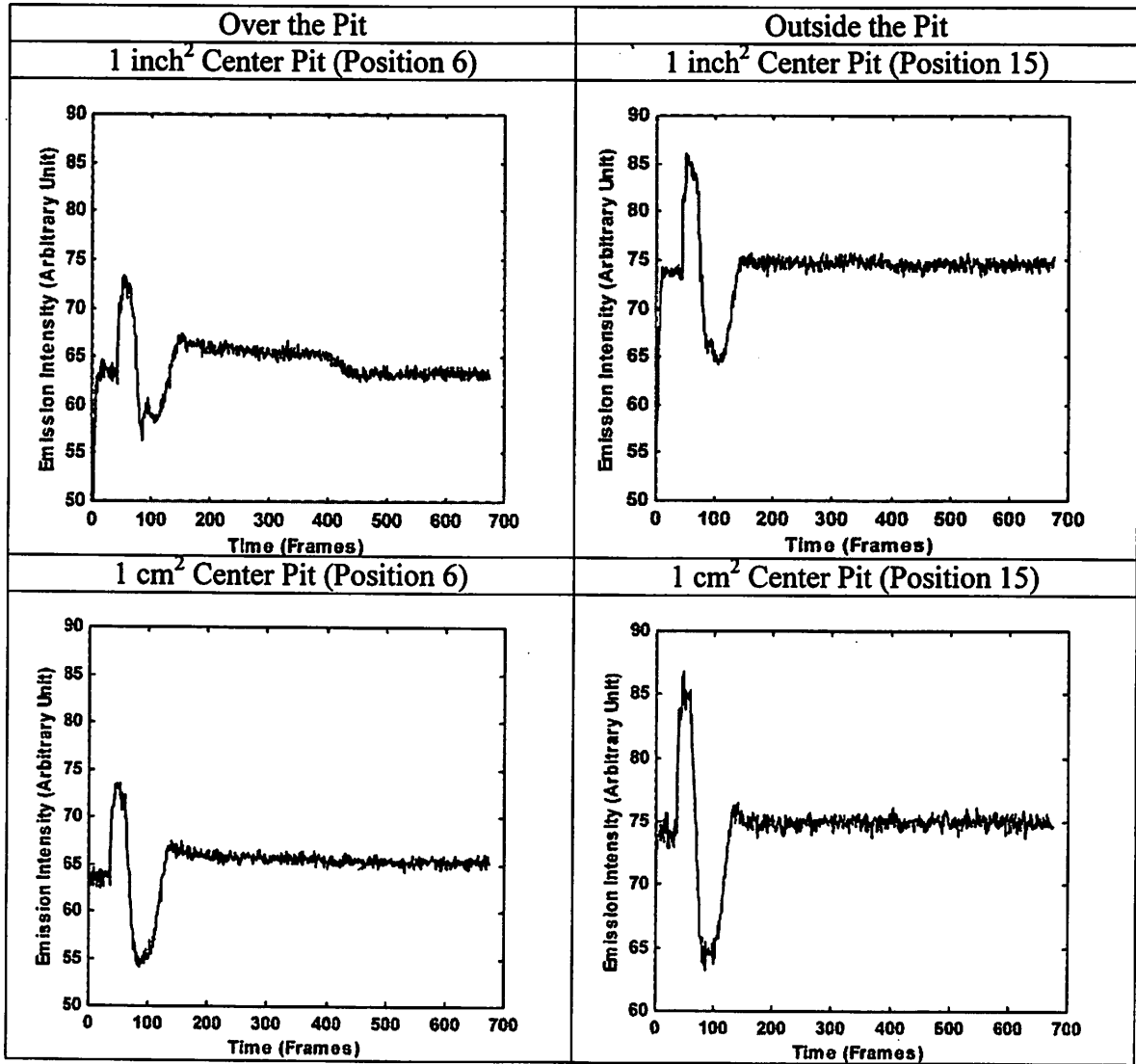


Figure 14. Layer transition signals (average intensity of the selected wavelengths) at different points on a wafer: above the pit and outside the pit. 1 inch² and 1 cm² center pit etching

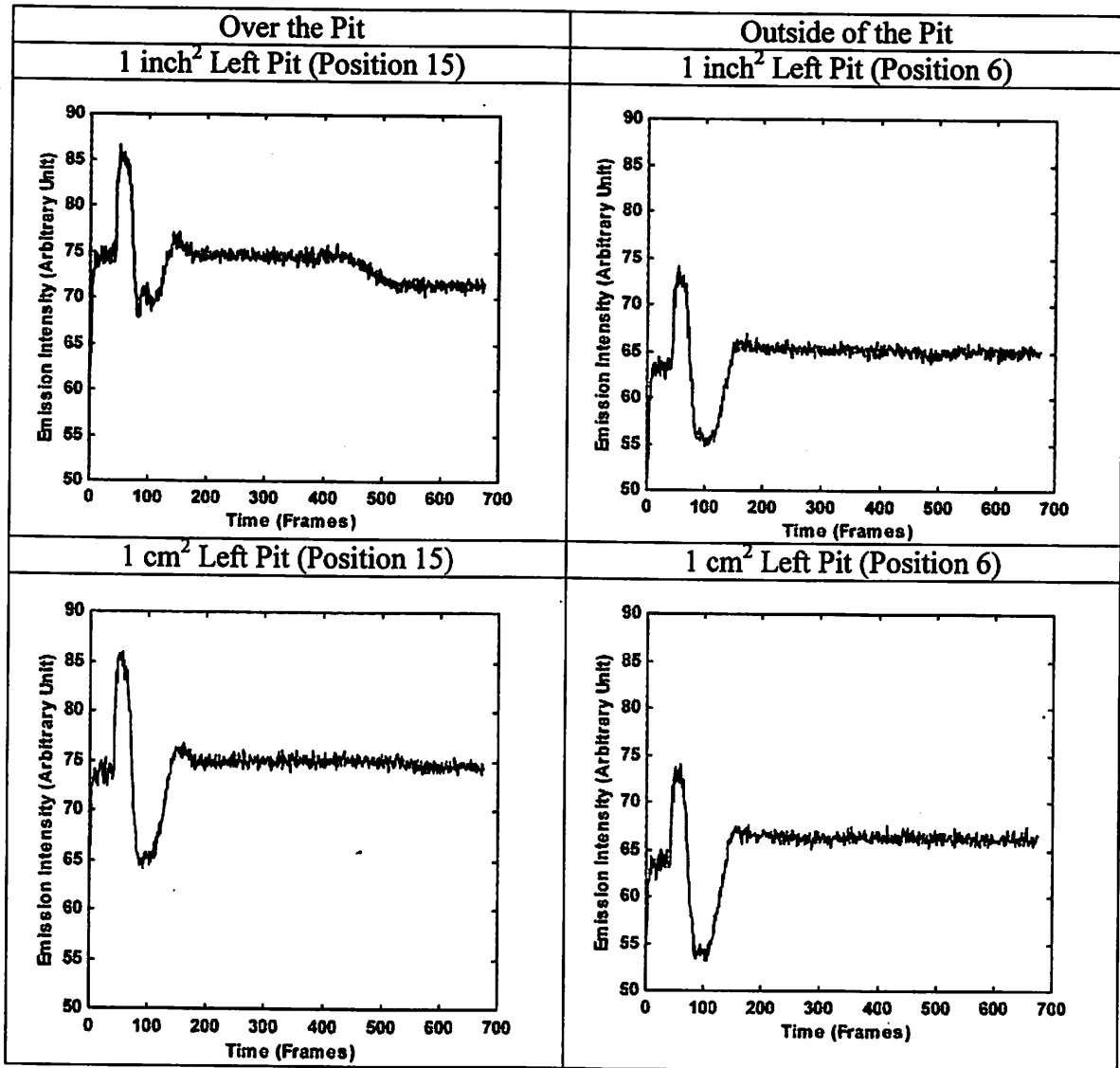


Figure 15. Layer transition signals (average intensity of the selected wavelengths) at different points on a wafer: above the pit and outside the pit. 1 inch² and 1 cm² left pit etching.

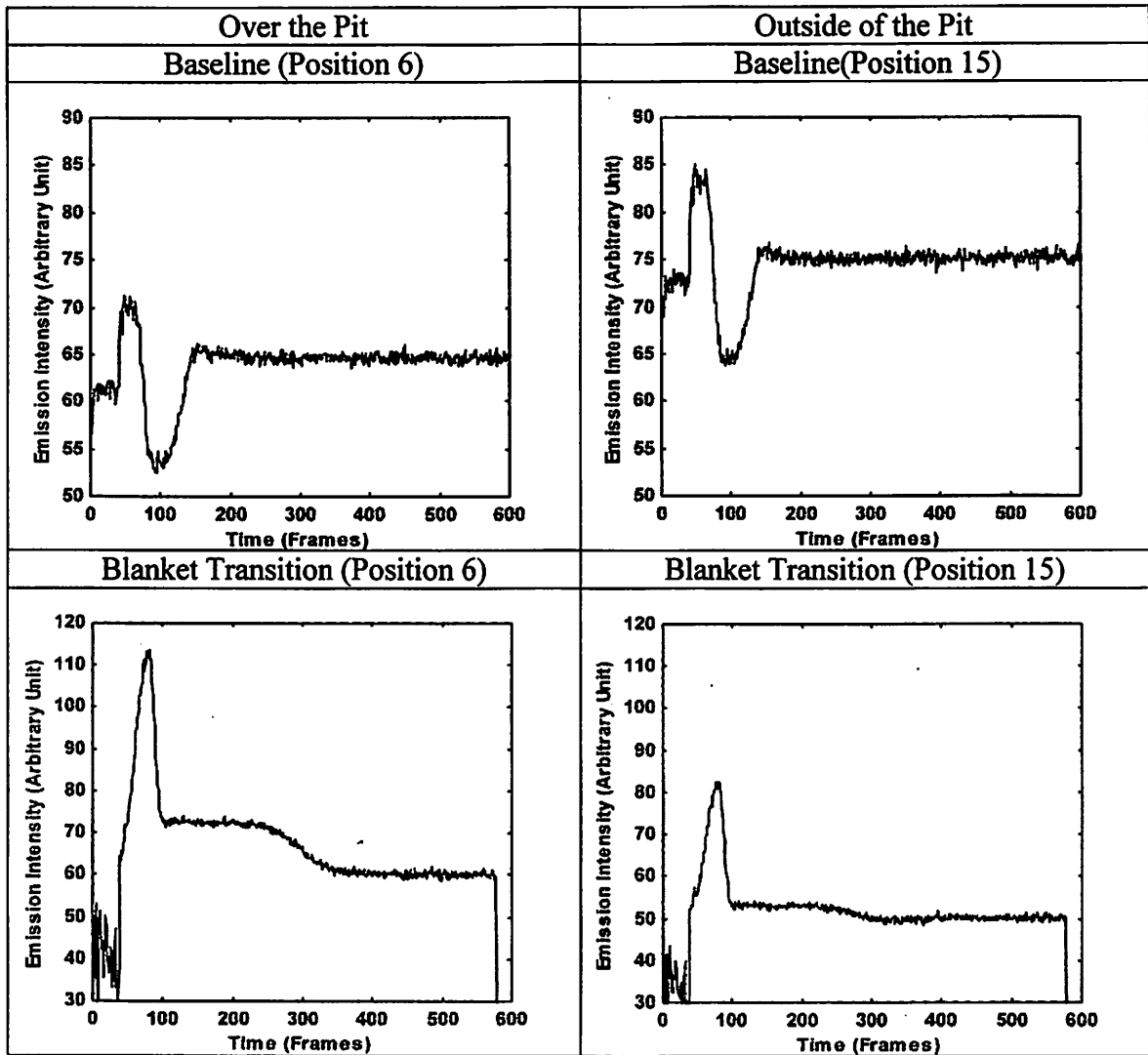


Figure 16. Layer transition signals (average intensity of the selected wavelengths) at different points on a wafer: above the pit and outside the pit. Baseline and blanket wafer etching.

As mentioned earlier, it turned out that the baseline wafer signal levels during main etching did not vary much compared to the amount of signal changes occurred during end-point transitions. Therefore, baseline wafers were excluded from the analysis. Figure 17 illustrates the typical signal variation and noise during etching, after initial signal fluctuations, at a single angle.

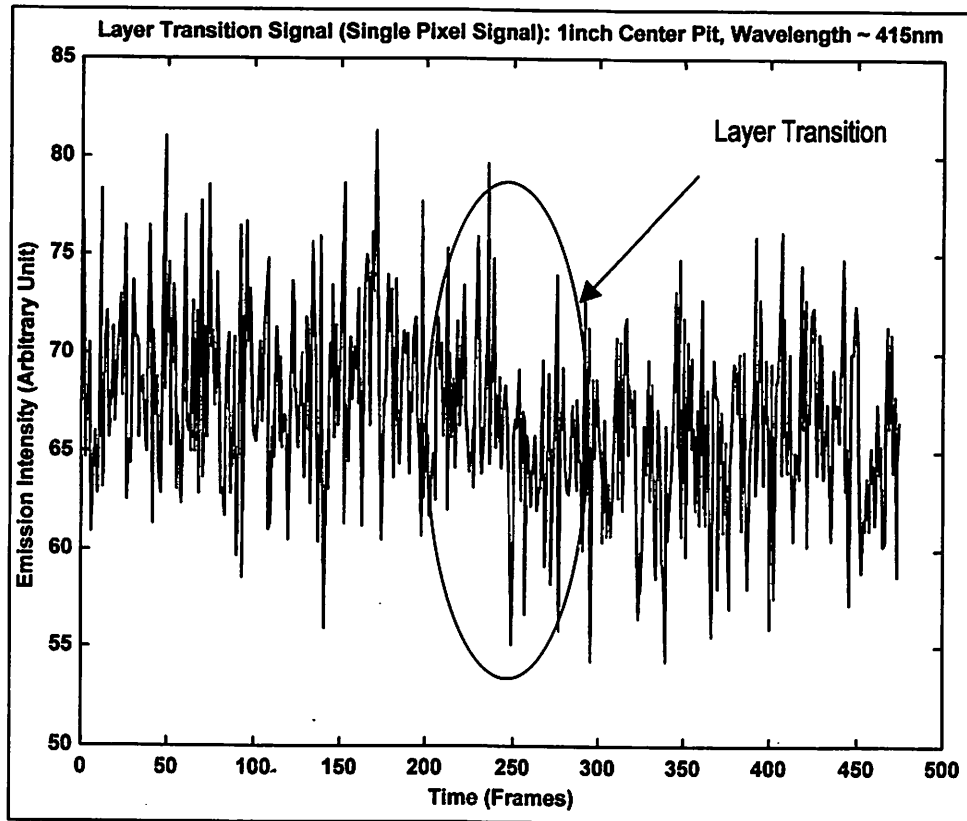


Figure 17. Single pixel signal variation during a layer transition

Since a large amount of wavelength information was available, Principal Component Analysis (PCA) was performed in order to summarize the data. Table 2 shows the amount of variation explained by each principal component. The first principal component of each wafer explains almost all variations occurring in the data set. Figures 18 through 25 show the first four principal component scores of the wafers listed in Table 2. Figures 26 through 29 are the corresponding loadings for each type of wafers.

Table 2. Normalized Eigenvalues for first 5 principal components

| Pit Type/Location | Principal Component | 1st | 2nd | 3rd | 4th | 5th |
|--------------------------|----------------------------|------------|------------|------------|------------|------------|
| 1-Inch/ Left | Normalized Eigenvalues (%) | 99.58 | 0.02 | 0.01 | 0.01 | 0.01 |
| 1cm/ Left | Normalized Eigenvalues (%) | 99.63 | 0.01 | 0.01 | 0.01 | 0.01 |
| 1-Inch/ Center | Normalized Eigenvalues (%) | 99.63 | 0.01 | 0.01 | 0.01 | 0.01 |
| 1cm/ Center | Normalized Eigenvalues (%) | 99.65 | 0.01 | 0.01 | 0.01 | 0.01 |

Due to the strong dominance of first principal components, only the first principal components were selected for end-point detection. Figure 30 through 35 show the normalized first principal component score surface and contour plots. The figures describe the first principal component scores as a function of time (in frames) and angular position, for untreated data and filtered data.

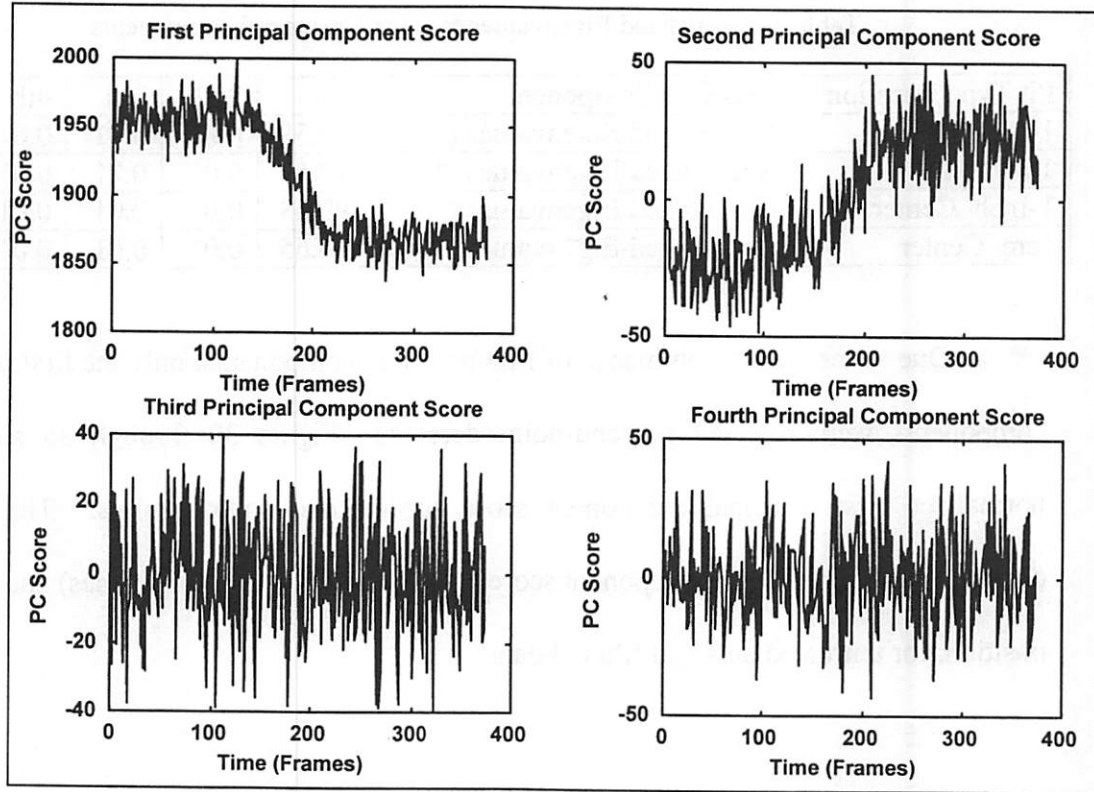


Figure 18. Principal component scores from a 1-inch left-pitted wafer. Angular position: 15 (over the pit)

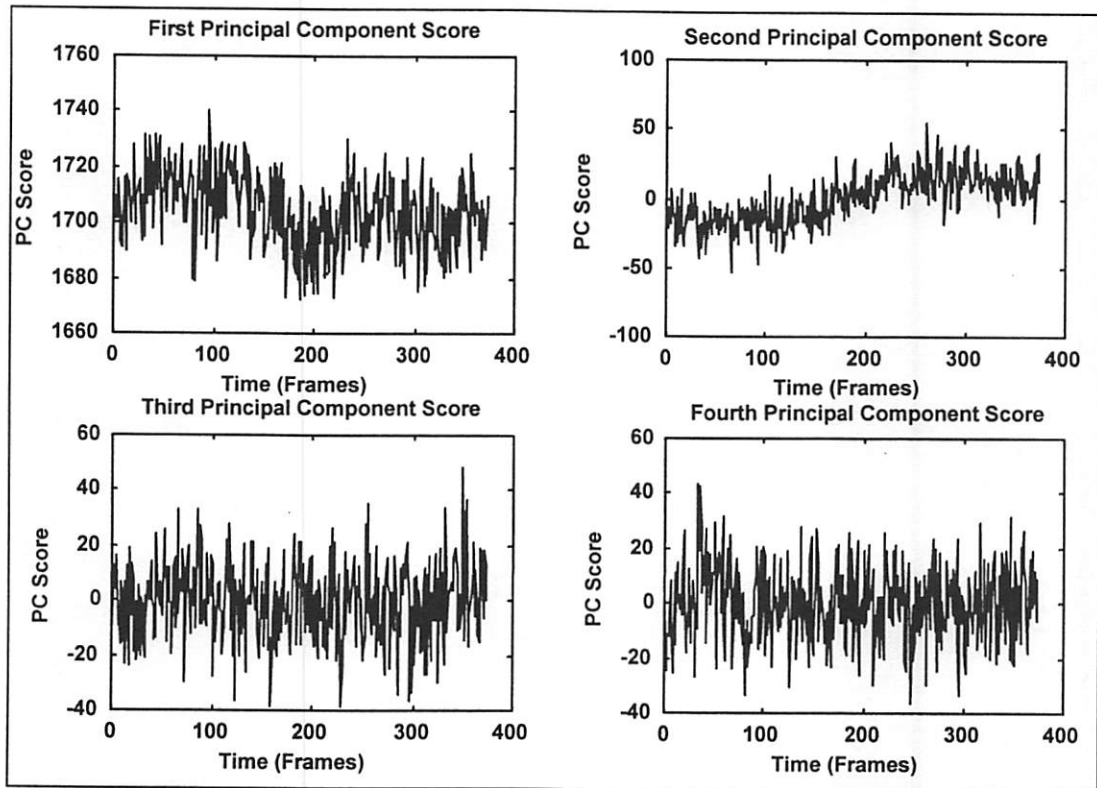


Figure 19. Principal component scores from a 1-inch left-pitted wafer. Angular position: 6 (outside the pit)

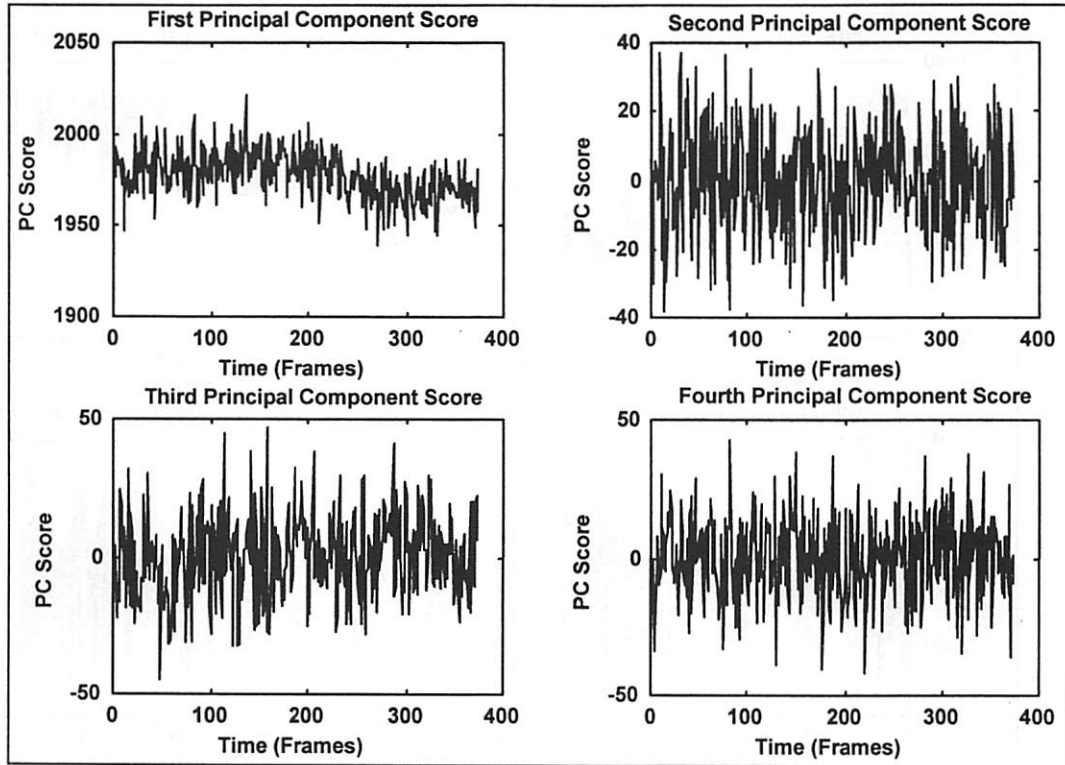


Figure 20. Principal component scores from a 1cm left-pitted wafer. Angular position: 15 (over the pit)

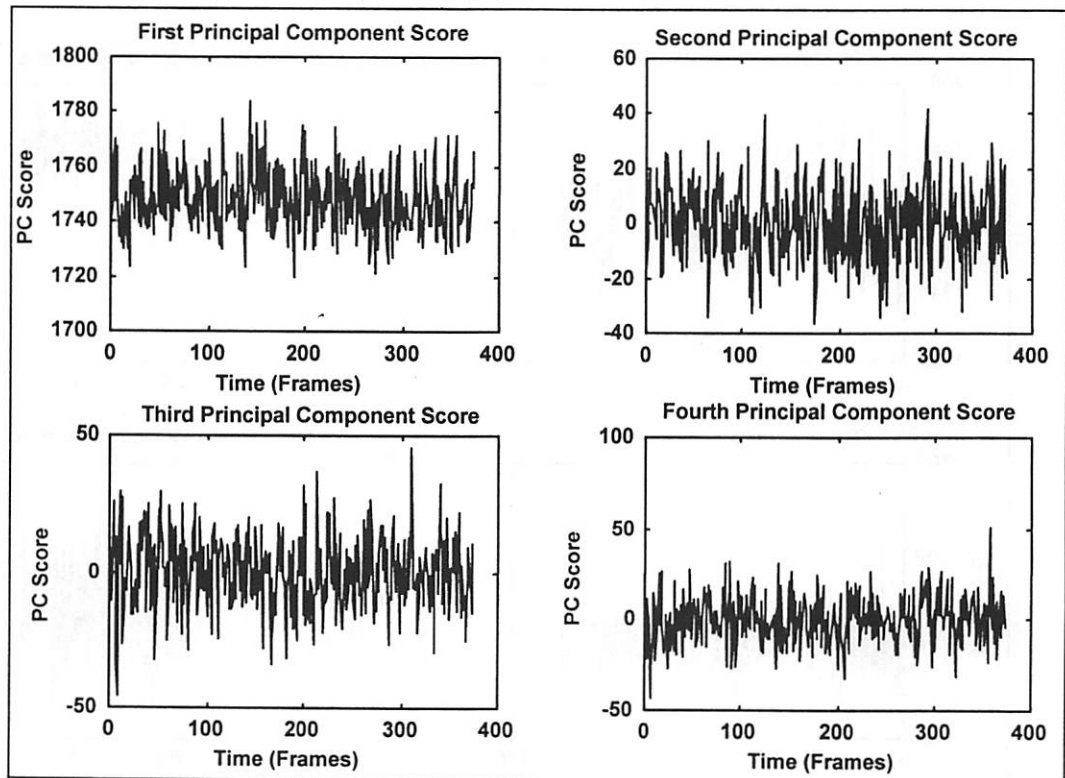


Figure 21. Principal component scores from a 1cm left-pitted wafer. Angular position: 6 (outside the pit)

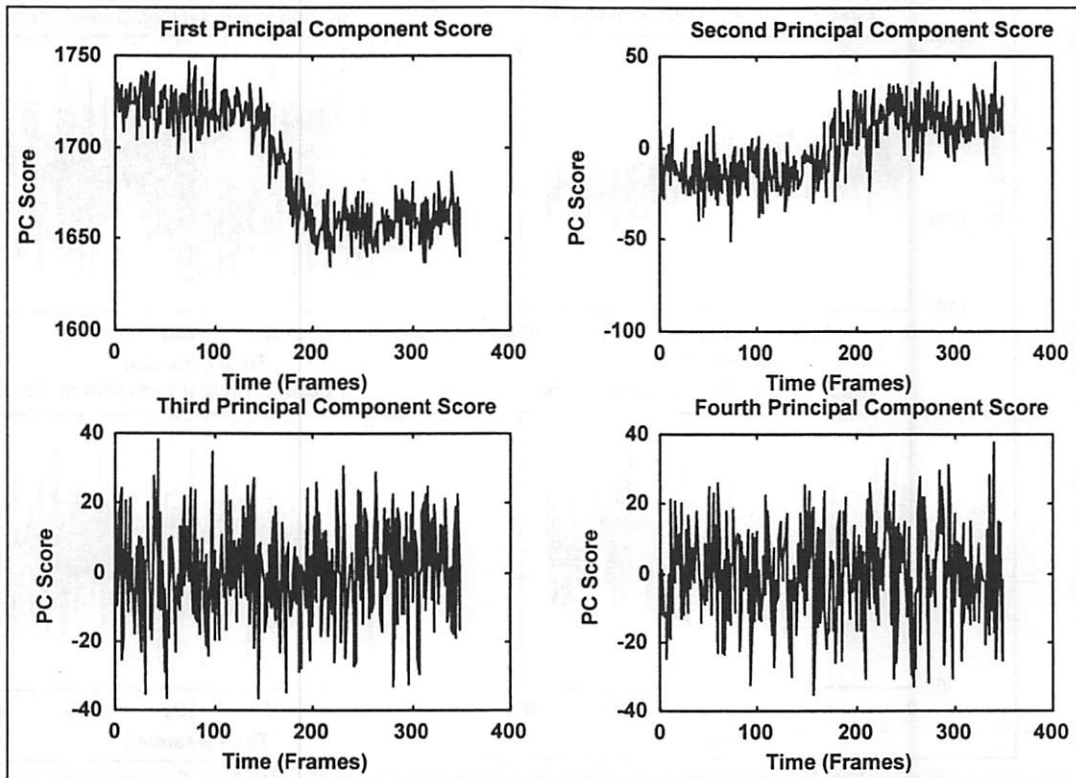


Figure 22. Principal component scores from a 1-inch center-pitted wafer. Angular position: 6 (over the pit)

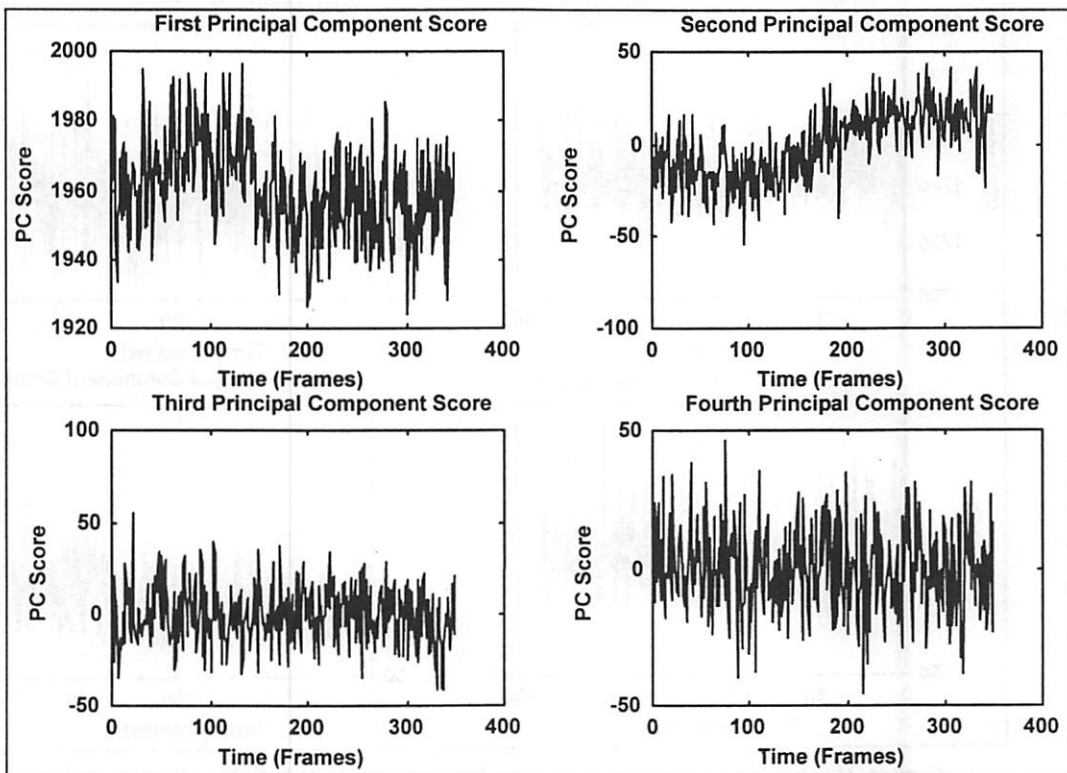


Figure 23. Principal component scores from a 1-inch center-pitted wafer. Angular position: 15 (outside the pit)

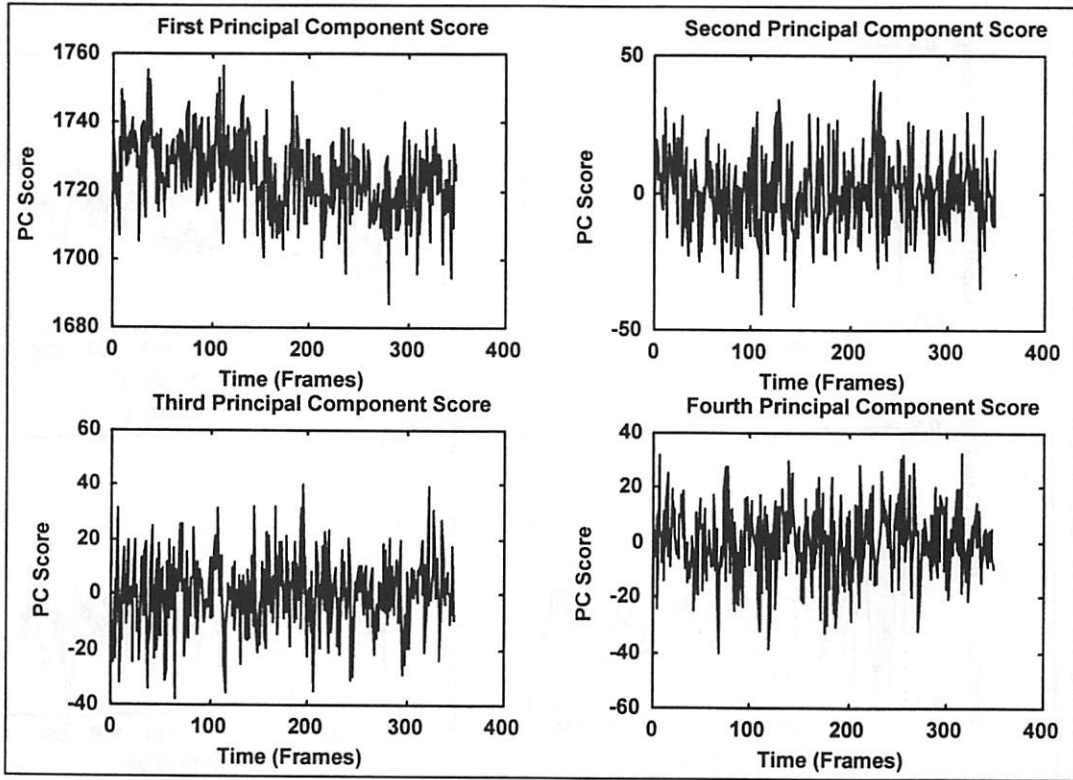


Figure 24. Principal component scores from a 1cm center-pitted wafer. Angular position: 6 (over the pit)

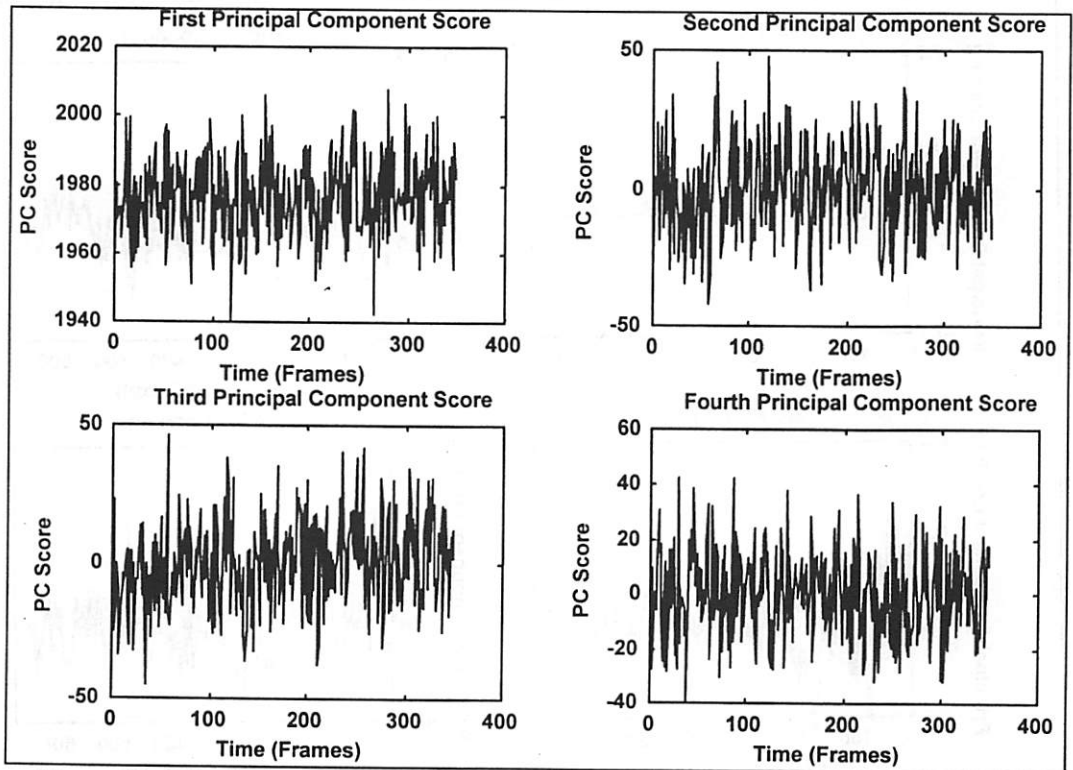


Figure 25. Principal component scores from a 1cm center-pitted wafer. Angular position: 15 (outside the pit)

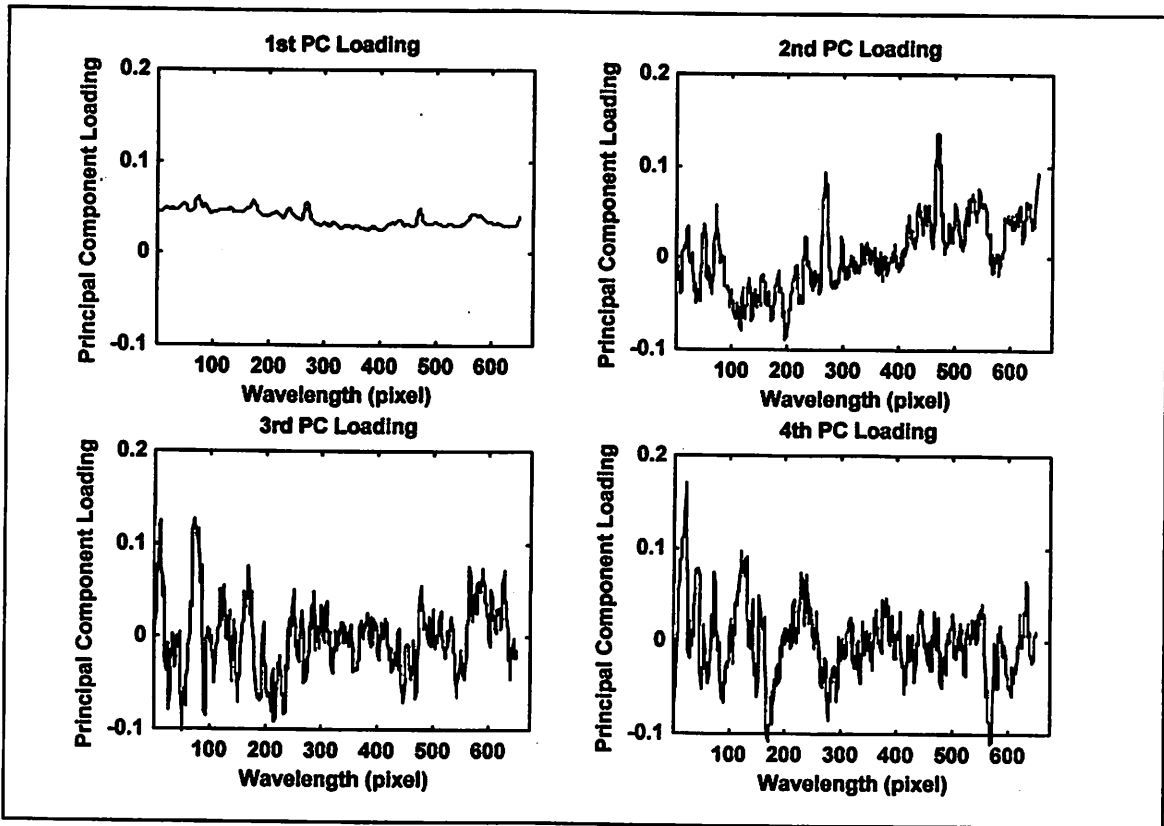


Figure 26. Principal component loadings for 1-inch left-pitted wafer. Angular position: 15

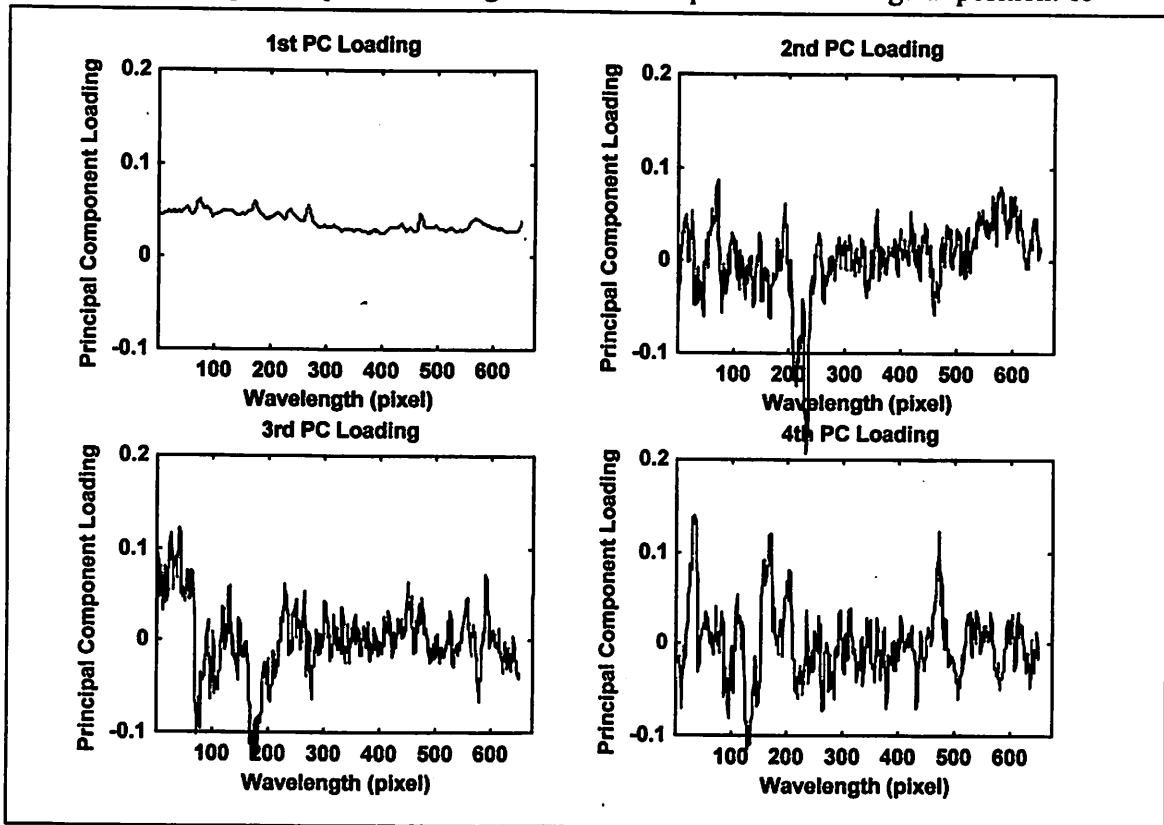


Figure 27. Principal component loadings for 1cm left-pitted wafer. Angular position: 15

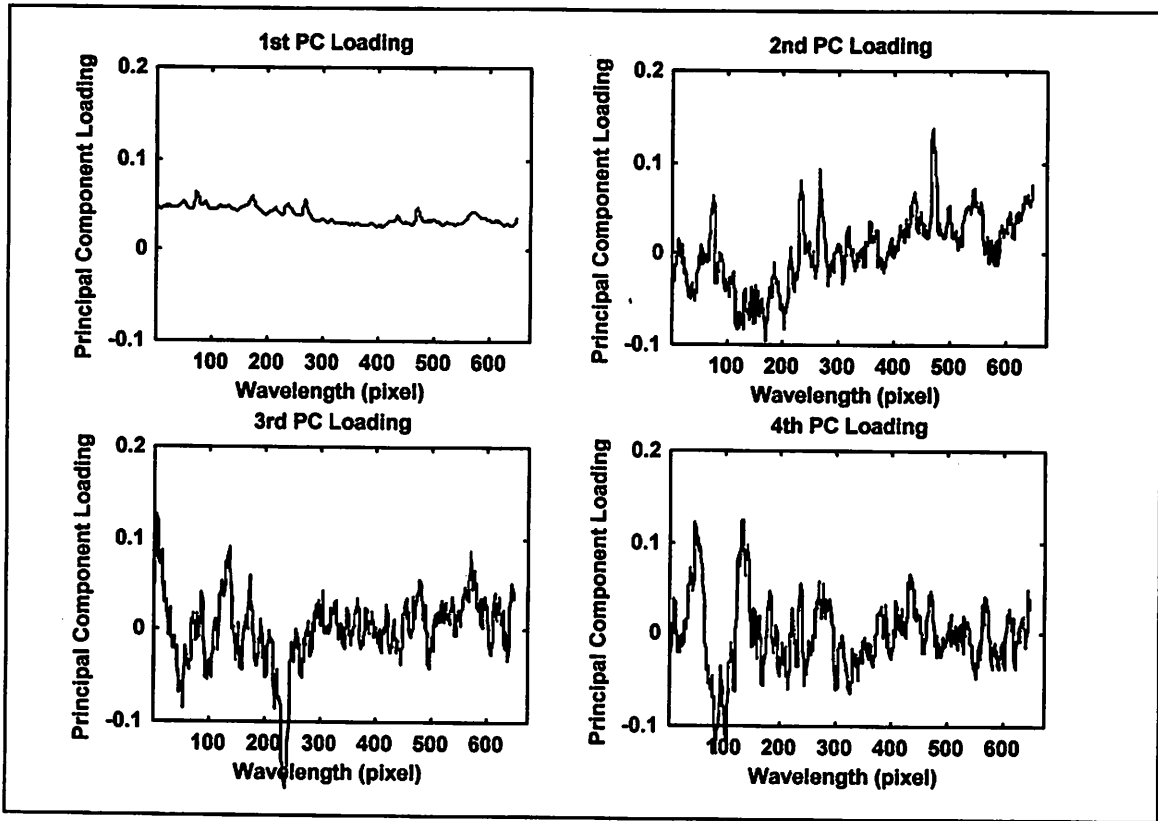


Figure 28. Principal component loadings for 1-inch center-pitted wafer. Angular position: 6

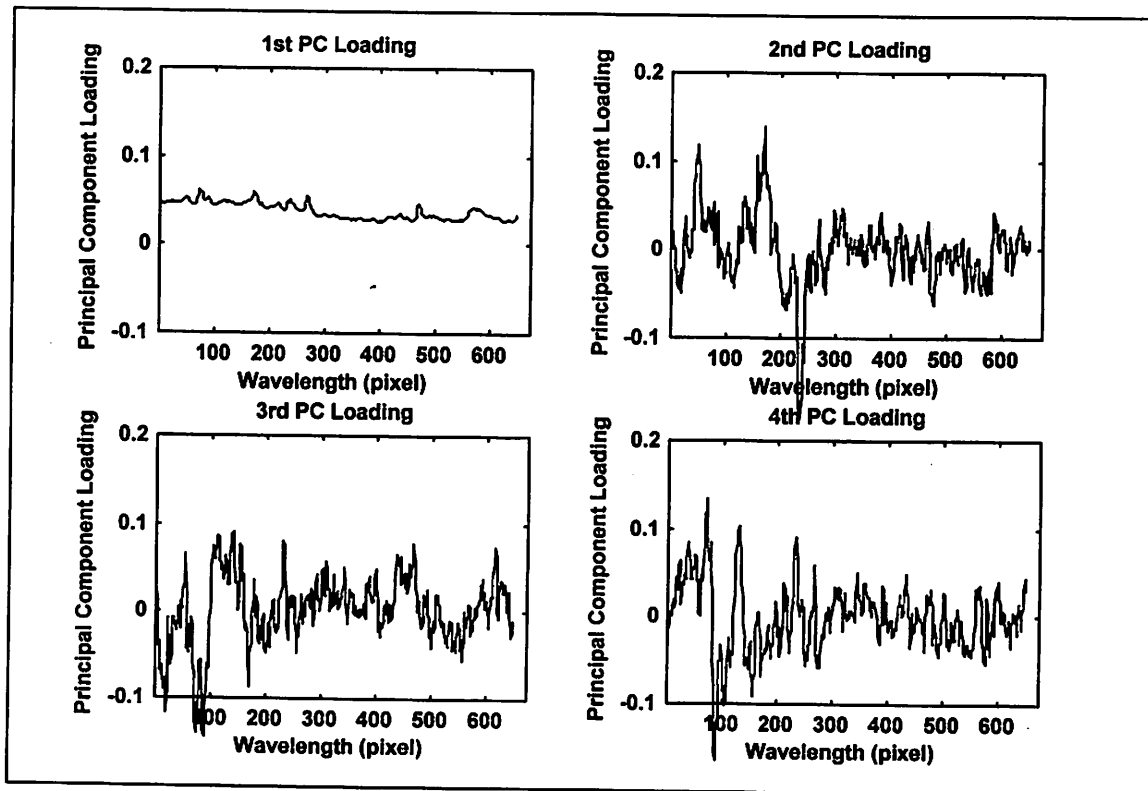


Figure 29. Principal component loadings for 1cm center-pitted wafer. Angular position: 6

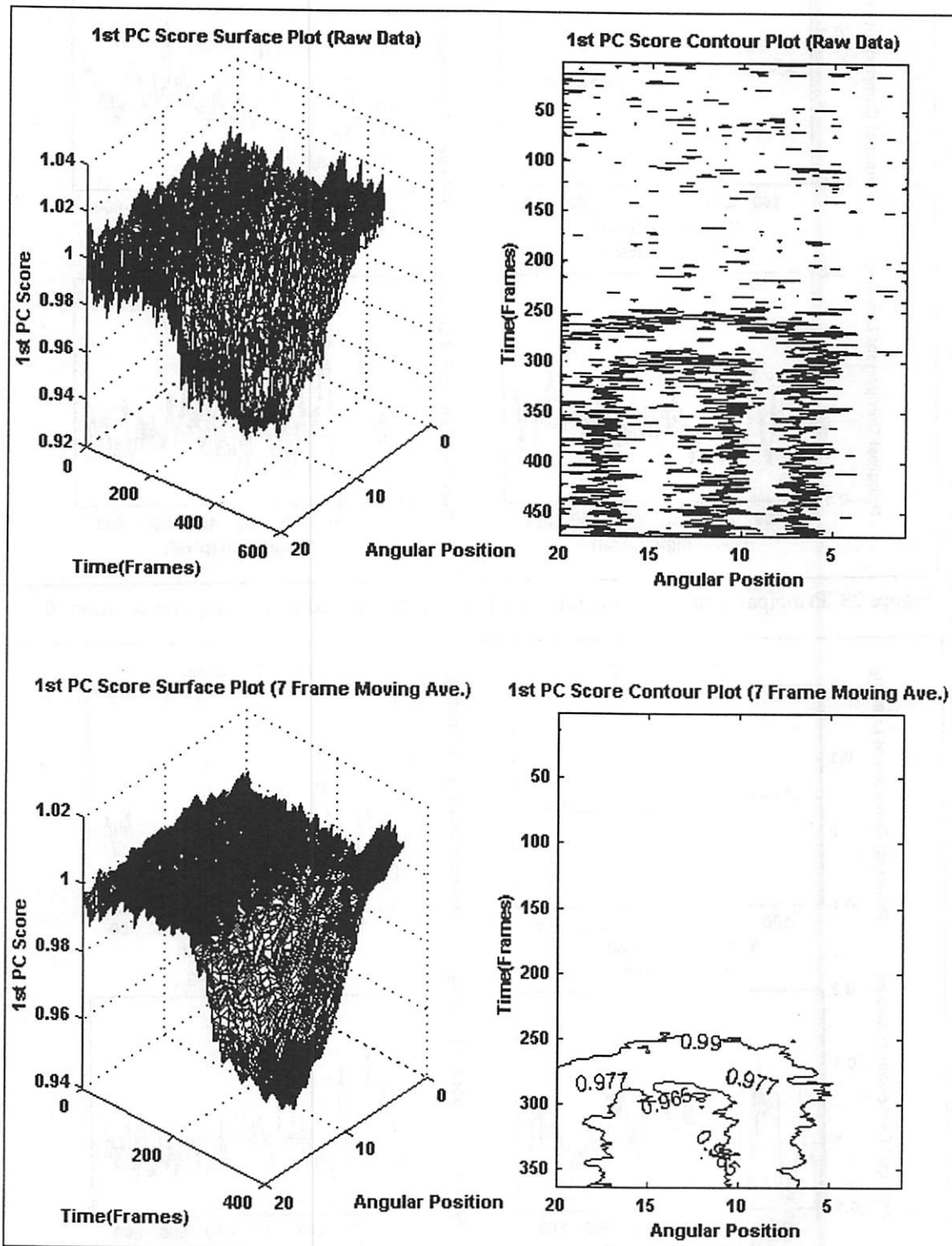


Figure 30. Surface and contour plot of a 1-inch left-pitted wafer.

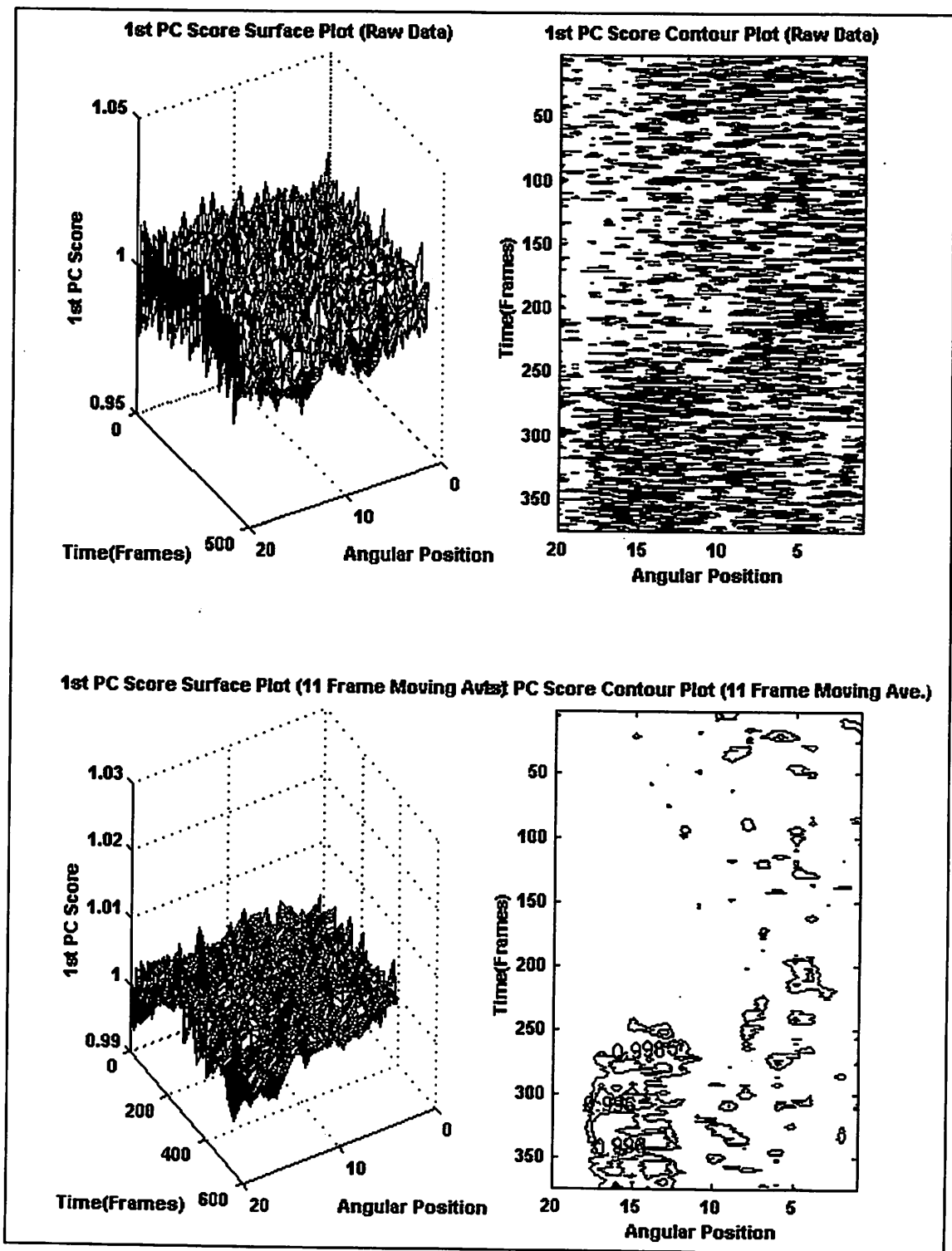


Figure 31. Surface and contour plot of a 1cm left-pitted wafer.

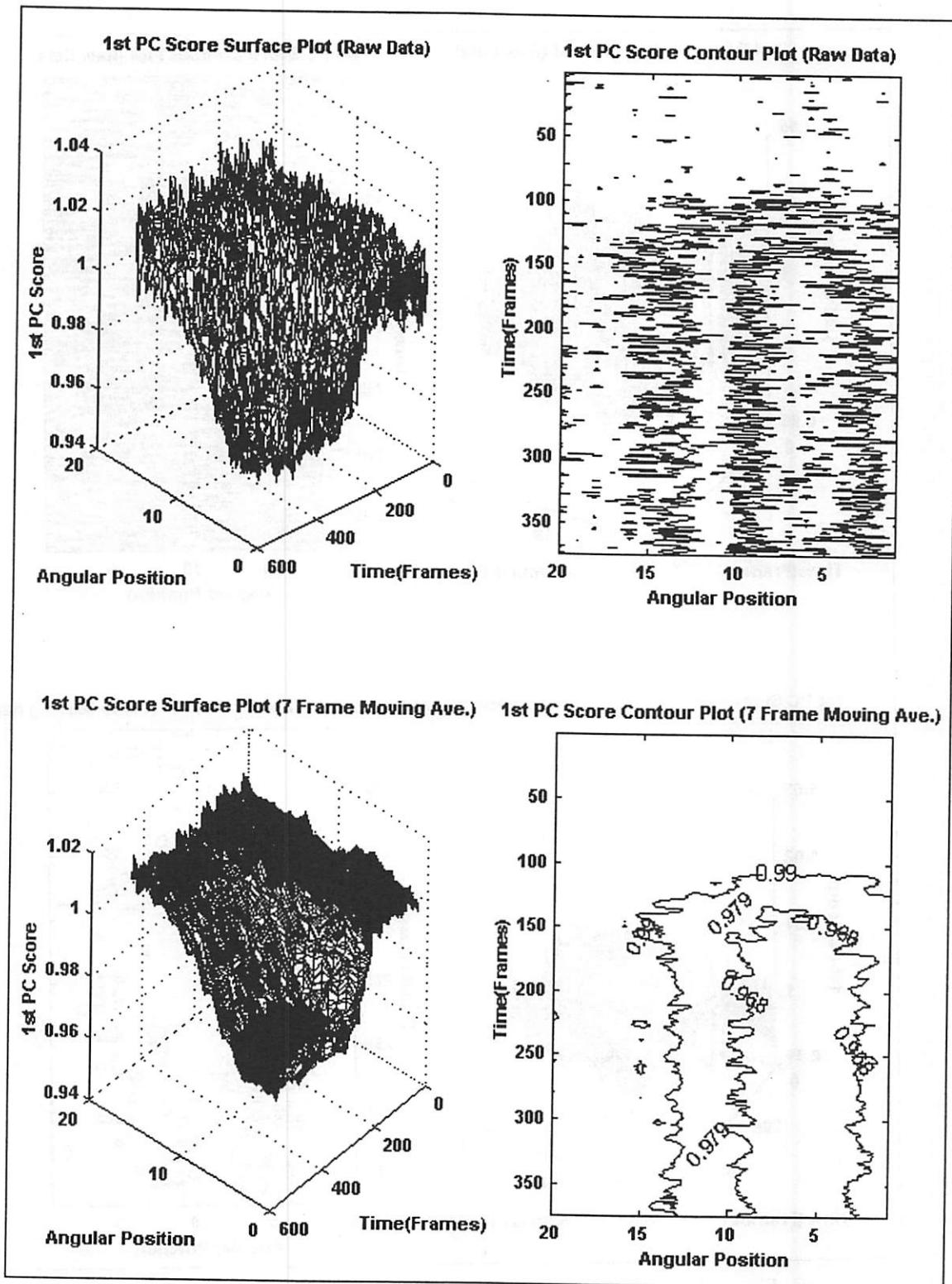


Figure 32. Surface and contour plot of a 1-inch center-pitted wafer.

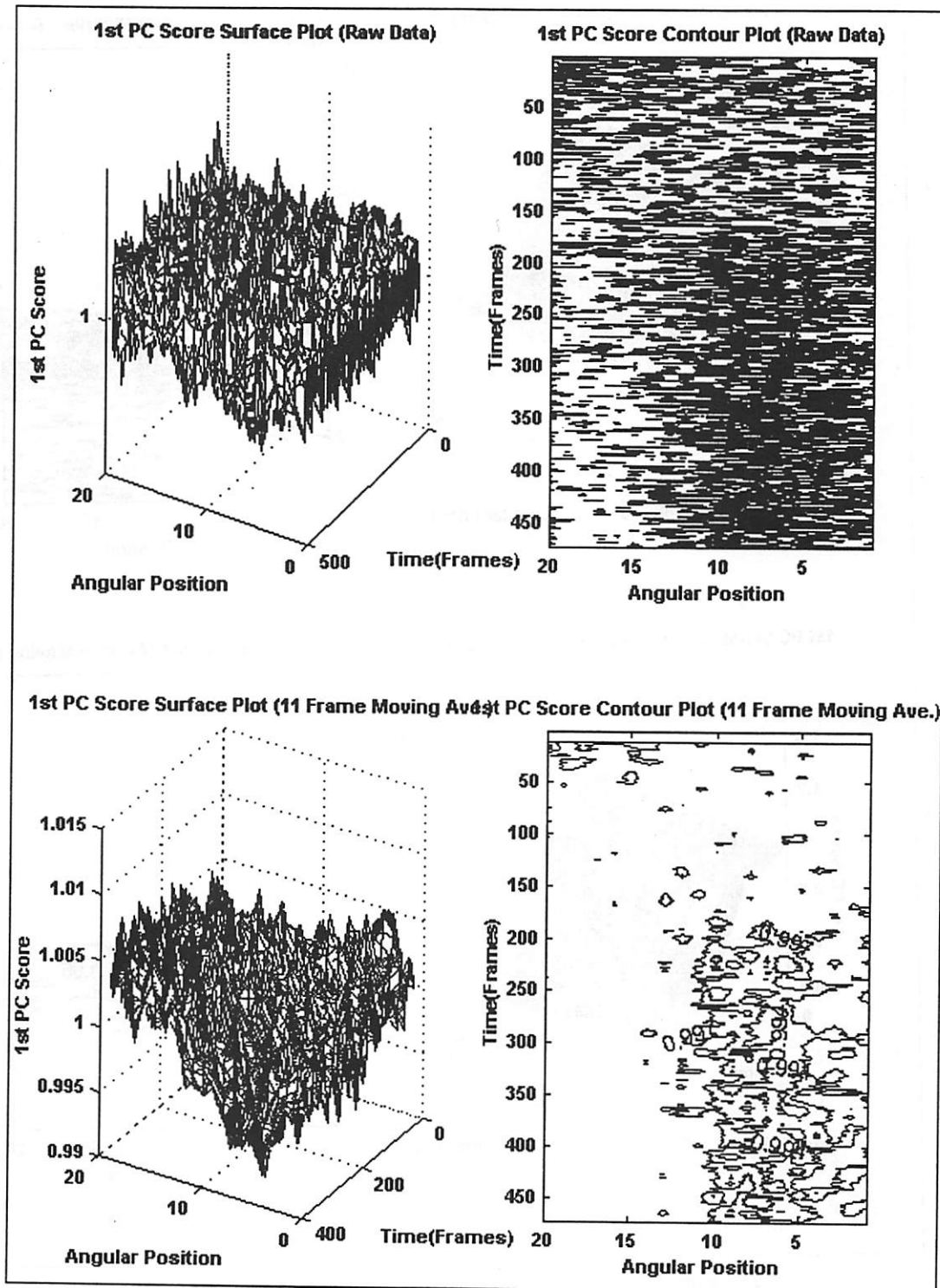


Figure 33. Surface and contour plot of a 1cm center-pitted wafer.

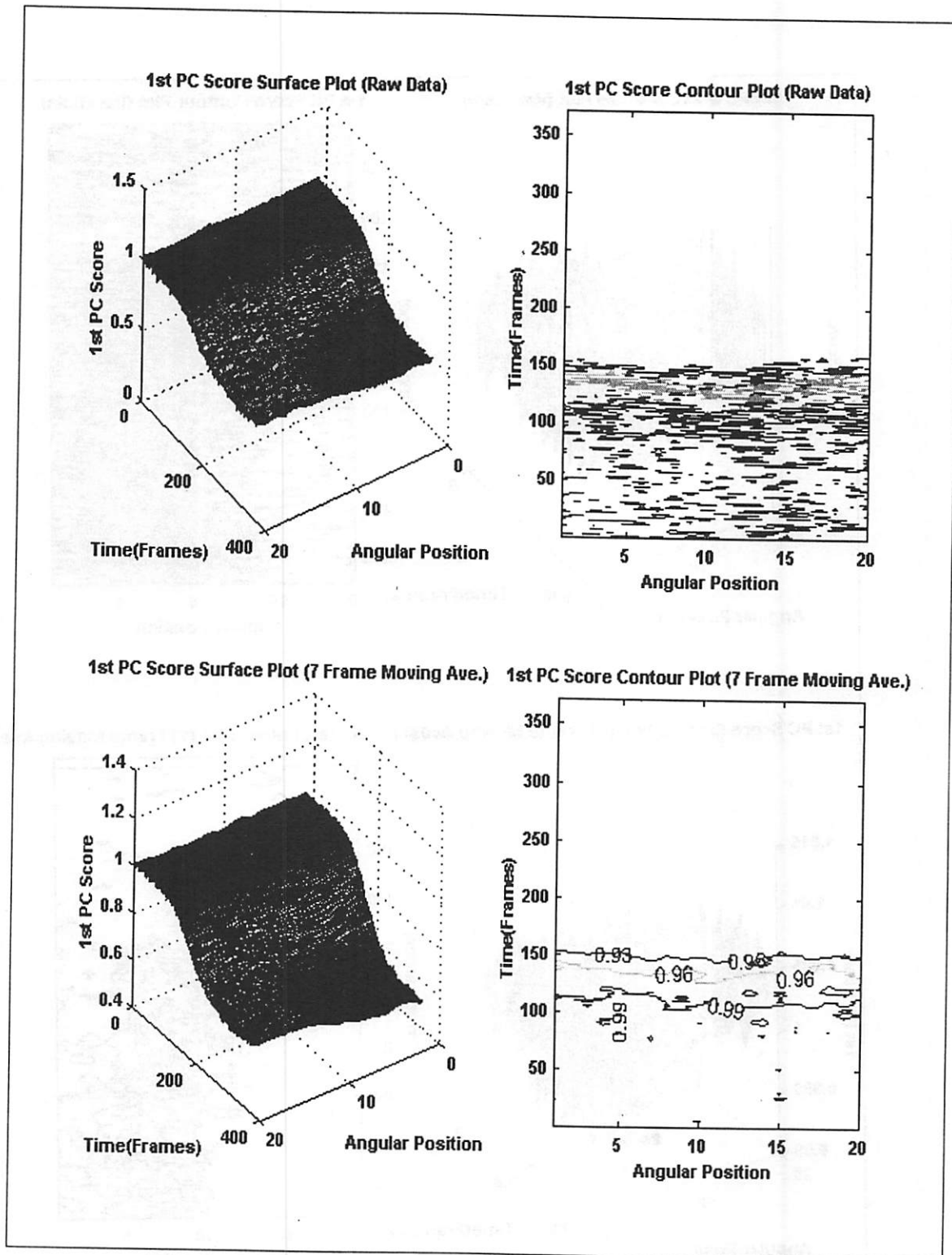


Figure 34. Surface and contour plot of a blanket wafer.

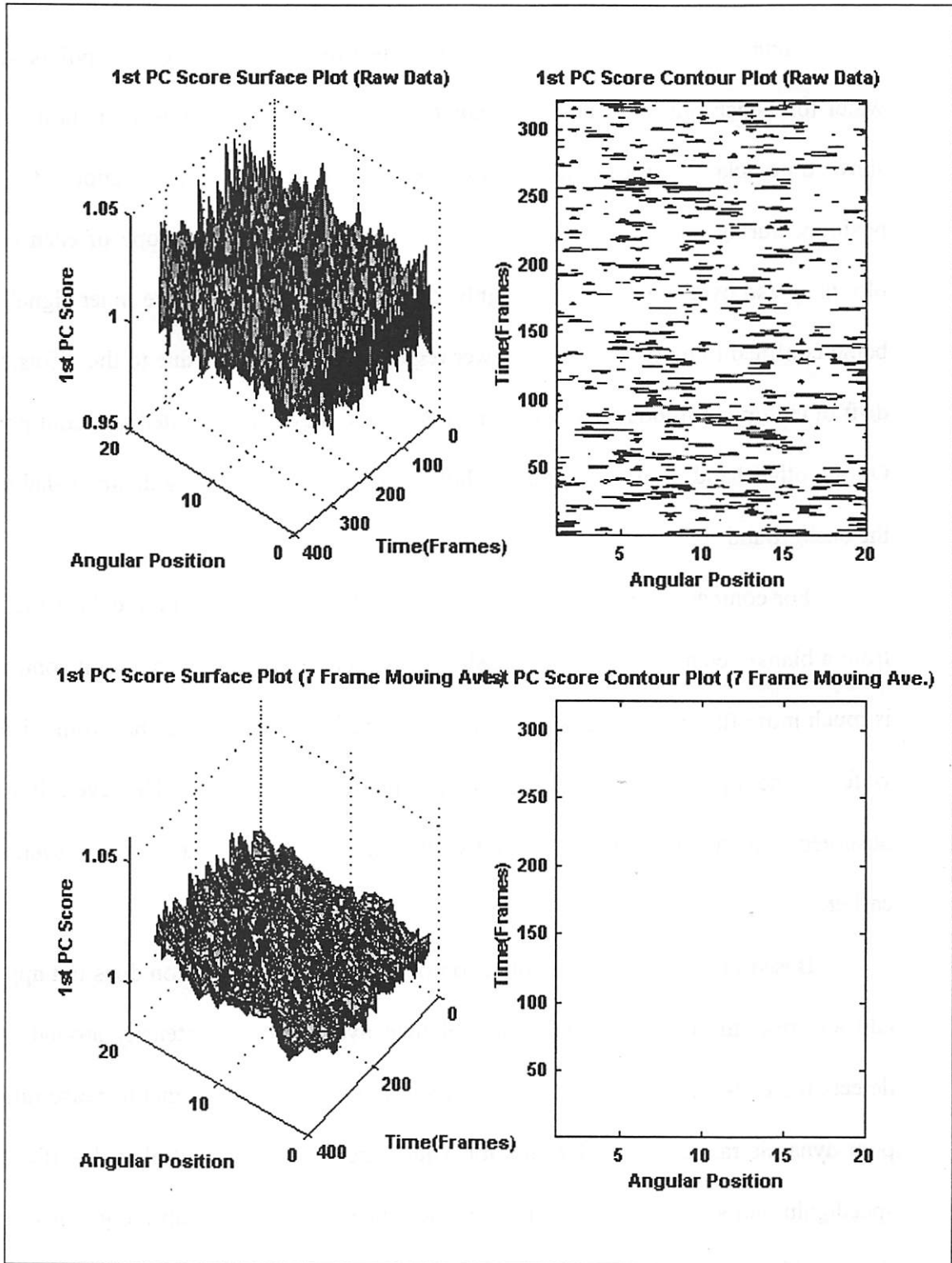


Figure 35. Surface and contour plot of a baseline wafer (no end-points).

Figures 30 and 32 show that we can detect the occurrences of end-points across a wafer for 1-inch pits, at a fine time scale (33ms/frame). The contour plots in the figures show time-delayed spread of principal component scores as a function of angular position, during end-point transitions. The outermost signal envelope of each contour plot is spread over a distance of roughly 2 inches with the successive inner signal levels being confined to narrower and narrower regions. This might be due to the diffusion and drift of etching by-products to the pit region, where they get re-excited and emit photons. On the other hand, Figure 31 and 33 show that 1cm pits are barely distinguishable over the background signal. ✓

For comparison purposes, Figure 34 and 35 are included. Figure 34 is the signal from a blanket etching. As the figure shows, the curvature of each end point contour line is much more flat than pitted wafers cases. Figure 35 contains the signal from a baseline wafer. The figure does not have any end-point occurrences. However, it can be observed that the signal levels do not drift much during etching as it has been stated earlier.

Based on the results, the collection of wavelength information does not appear to add any new information. Only the weighted average signal intensity around 405nm detects the end-point transitions. This might be due to the low signal to noise ratio and poor dynamic range of the CID detector, which are the direct result of trade-off between speed/gain and signal to noise ratio/dynamic range. Therefore, with the given situation, the combination of a band-pass or notch filter with a one-dimensional CCD or photodiode array can provide a better result. This scheme eliminates the use of the spectrograph. The elimination of the spectrograph accomplishes two things: higher

plasma emission intensity at the sensor and reduction in the required data throughput. The higher plasma emission intensity can be expected since there is no diffraction grating involved, which spreads out the emission across the horizontal dimension of the CID. The reduction in the data throughput creates a room for improvement in dynamic range.

Chapter 4

Introduction: Tomography

4.1 Motivation

Based on the results from the previous section, it was determined that time-resolved end-point transitions with 1 inch² pits could be detected, which represented about 8% of the wafer area. This experiment was performed on test wafers that had about 90% open space. 1-cm² pits, which represented about 1.2 % of the wafer area, were barely visible. Given the strength of the signal, it most likely was possible to detect pits that were about 5% of the wafer area. The measurements provided one-dimensional projections across the wafer as the setup in Figure 7 showed.

Tomography adds another dimension to this. Two-dimensional, time-resolved end-point maps can be used in the process characterization and detection of end-points across wafers. The availability of two-dimensional emission maps can add valuable real-time information for a real-time or run-to-run control of the etching recipes.

4.2 Tomography Applications

2D-computed tomography (CT) is used to reconstruct a two-dimensional image from a set of one-dimensional projections. Depending on the types of signals collected, x-ray, emission, thermal, ultrasonic, or electrical impedance CT is employed.

X-ray tomography is mainly used in the medical field for finding the locations of soft tissues and bones of a patient. Other applications include airport scanners, rock and fossil scanners. In x-ray CT, an x-ray source ($\sim 100\text{keV}$) rotates around a subject illuminating it from various angles. On the opposite side, an array of detectors collects the transmitted x-ray as shown in Figure 36. In a simplified model, assuming collimated x-ray beam is used, the measured photon density on the detector surface, $S_{out}(E)$, at energy E is related to the source photon density, $S_{in}(E)$, and the subject body attenuation coefficient, $\mu(x,y,E)$, in the following way:

$$S_{out}(E) = S_{in}(E) \cdot \exp\left[-\int \mu(x,y,E) ds\right] \quad (4.1)$$

In this case, the line integration is performed along the x-ray path. μ incorporates the attenuation due to photoelectric effect and Compton scattering [5]. In reality, a fan-beam based x-ray CT scanner shown in Figure 36 is used for a subject scan, for shorter scan time. A typical resolution of medical x-ray CT is about 1~2mm, and single-slice scans can take on the order of 10 seconds. Higher resolution systems can provide details down to $10\mu\text{m}$ [6].

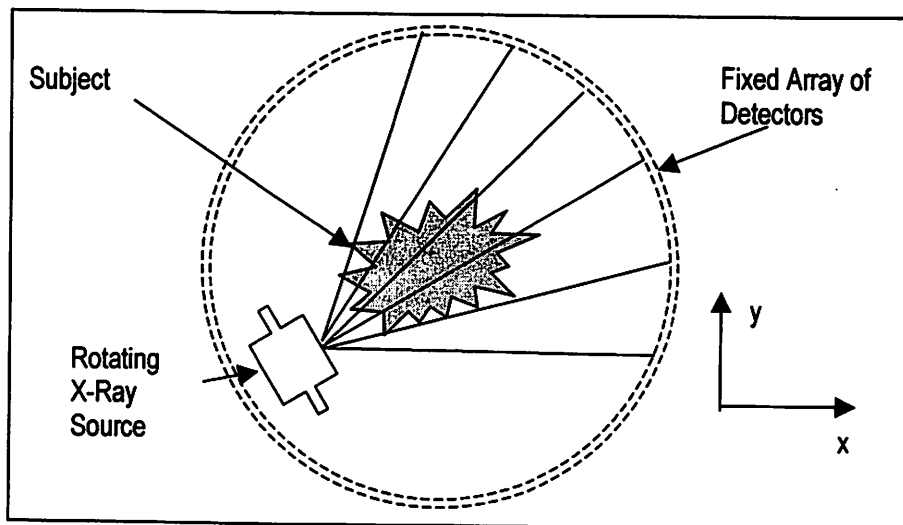


Figure 36. A fourth-generation x-ray tomography scanner schematics.

Unlike X-ray scanners, which are used to locate objects within the scan subject, emission CT is mainly used in the medical field to diagnose diseases on certain parts of a body. Brain activity, hemorrhage, or abnormal functionality of body parts can be selectively detected. In emission CT, radioactive tracer is positioned inside the body of a subject through injection, ingestion, or inhalation. Depending on the types of radioactive decay, two emission CT scanners are available. Single photon emission computed tomography (SPECT) refers to the case where a single gamma-ray photon ($\sim 140\text{keV}$) is created as a result of a single radioactive decay. Since the source intensity, which is dependent on the tracer concentration inside the subject's body, is not known, more elaborate reconstruction scheme is required. This results in blurrier reconstructed images. Also, the position of the source is not localized in SPECT, since gamma rays from different body locations can converge on the same detector location. Therefore, a collimator is used in front of the detector array to gather only the photons coming at a certain angle to the detector surface. However, the usage of the collimator decreases the photon flux and contributes to poorer spatial resolution compared to positron emission tomography (PET) scanners. All things considered, SPECT can deliver about 7mm spatial resolution [7].

Positron emission tomography (PET) scanners, on the other hand, are based on positron emissions during radioactive decays. The positrons interact with electrons after traveling a short distance ($\sim 1\text{mm}$). They get annihilated into pairs of photons ($\sim 511\text{keV}$) traveling at roughly 180 degrees from each other. This unique emission condition is used to detect the location of the emission using coincidence circuits as shown in Figure 37. For example, detectors A and B on Figure 37 collect emission signals simultaneously

when a pair of photons is generated along the line joining the two detectors and parallel to the line. Therefore a collimator is not needed for PET scanners and higher resolution is possible [7].

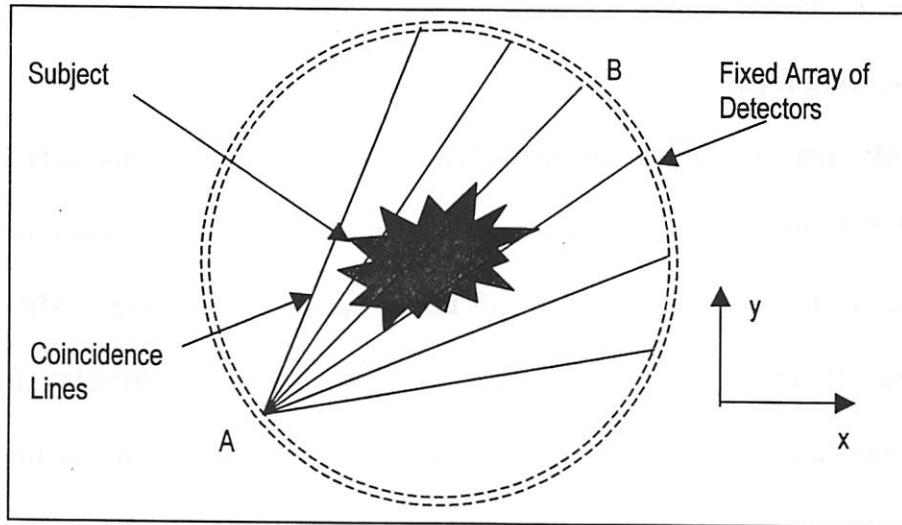


Figure 37. Positron emission tomography scanner schematics.

Ultrasonic scanners detect an interface between two layers. Main applications include finding the positions of objects and detecting object movements such as blood or water flow, fetus movements using obstetric ultrasound scan, and fire spread study. Also, ultrasonic CT can deliver real-time images, which are not done using x-ray or emission CT scanners. An Ultrasonic CT scanner measures frequency shift, pressure, and/or delay of the transmitted or reflected acoustic wave ($> 20\text{KHz}$). From those signals, positions of internal objects, obtained from cross sectional attenuation coefficients or refractive indices, can be found. In particular, delay time, T_d , of the transmitted signal is related to the refractive index, $n(x,y)$, of the media in the following way:

$$\int [1 - n(x, y)] ds = V_w \cdot T_d \quad (4.2)$$

Here, V_w represents the propagation velocity of the medium surrounding the subject, which is usually water. The line integration is performed between the transmitter and detector. For attenuation coefficient calculation, several methods are available including energy-ratio method, division of transforms followed by averaging method, and frequency-shift method [5].

Magnetic resonance imaging (MRI) scanners are predominantly used in the medical field to detect blood flow to organs and their abnormal conditions. Tumors, cartilage, tendon, muscle, and other soft tissues can also be detected. MRI utilizes ^1H , ^{13}C , ^{23}Na , ^{31}P , or ^{39}K , which are elements present in water or responsible for biological energy transfers or nervous system activities. MRI is performed in the following way. First, a strong static magnetic field is applied to the patient's body. This aligns the magnetic moments of the above elements within the patient's body to the static field and results in a slight magnetization. Second, another magnetic source applies a radio frequency (RF) field to the patient, at a magnetic resonance frequency of the element desired. This tilts the magnetic moment of the element. The selected elements absorb the energy of the applied field and move up to higher energy states. However, due to the effects from the neighboring nuclei, magnetic moments become out of phase. The constant that characterizes this process is called transverse or spin-spin relaxation time. Finally, the RF field is turned off and the energy stored is released by the elements while they return to the equilibrium states. The time constant that characterizes this process is called longitudinal or spin-lattice relaxation time. Spin-density, Spin-spin relaxation time, and spin-lattice relaxation time are the main parameters used for the image reconstruction [5, 7].

Chapter 5

Tomography Simulation

5.1 General Tomographic Idea

The basic idea that applies to the plasma optical emission end-point detection is described in Figure 38. $f(x, y, t)$ represents the plasma emission intensity at a fixed height above the wafer at time t . $g_{\theta}(s, t)$ is the one-dimensional projection of $f(x, y, t)$ with θ degrees rotation from x-y coordinate. Assuming the optics and sensors employed can roughly collect parallel light rays, a data point in $g_{\theta}(s, t)$ is the strip (more precisely cylindrical or rectangular) integration of $f(x, y, t)$ in the r direction as shown in Figure 38. Obviously, emission details of $f(x, y, t)$ in r direction are lost in the process. Therefore, multiple measurements in various angles ($0^{\circ} < \theta < 180^{\circ}$) are needed in order to recover enough independent wafer emission information.

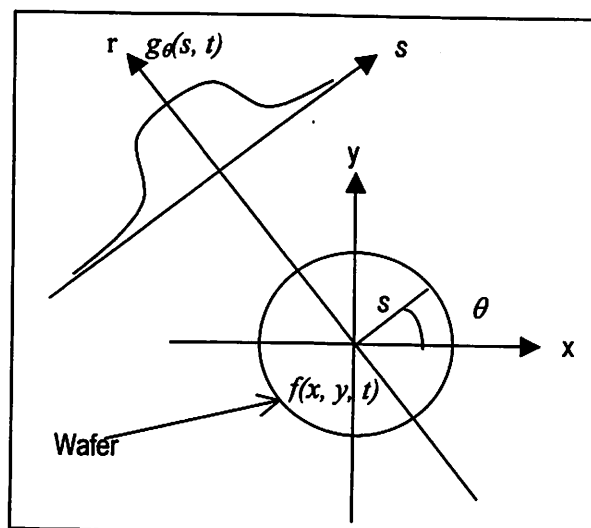


Figure 38. Plasma emission projection scheme.

For the reconstruction, filtered back projection can be used. The basic idea is that given the actual emission profile, $f(x, y, t)$, one-dimensional projections, $g_\theta(s, t)$, are measured.

$$g_\theta(s, t) = \int_{-\infty}^{\infty} f(s \cdot \cos \theta - r \cdot \sin \theta, s \cdot \sin \theta + r \cdot \cos \theta, t) dr \quad (5.1)$$

Then, the spatial Fourier transform of the projection is taken, where w is the spatial frequency for the projection angle θ . w implicitly represents two-dimensional spatial frequency.

$$G_\theta(w, t) = \int_{-\infty}^{\infty} g_\theta(s, t) \cdot e^{-j2\pi ws} ds \quad (5.2)$$

$$G_\theta(w, t) = \int_{-\infty}^{\infty} \left[\int_{-\infty}^{\infty} f(s \cdot \cos \theta - r \cdot \sin \theta, s \cdot \sin \theta + r \cdot \cos \theta, t) dr \right] \cdot e^{-j2\pi ws} ds \quad (5.3)$$

$$G_\theta(w, t) = \int_{-\infty}^{\infty} \int_{-\infty}^{\infty} f(x, y, t) \cdot e^{-j2\pi w(x \cos \theta + y \sin \theta)} dx dy \quad (5.4)$$

Let $u = w \cos \theta, v = w \sin \theta$. By defining the two dimensional Fourier transform as

$$G(w \cos \theta, w \sin \theta, t) = \int_{-\infty}^{\infty} \int_{-\infty}^{\infty} f(x, y, t) \cdot e^{-j2\pi w(x \cos \theta + y \sin \theta)} dx dy \quad (5.5)$$

We obtain

$$G_\theta(w, t) = G(w \cos \theta, w \sin \theta, t) \quad (5.6)$$

Therefore, if we take sufficient number of projections, we can estimate $G(u, v, t)$. Then, by applying the two dimensional inverse Fourier transform, we can recover $f(x, y, t)$.

$$f(x, y, t) = \int_{-\infty}^{\infty} \int_{-\infty}^{\infty} G(u, v, t) e^{j2\pi(ux+vy)} du dv \quad (5.7)$$

Since $du dv = w \cdot dw d\theta$, we obtain

$$f(x, y, t) = \int_0^{2\pi} \int_0^{\infty} G_{\theta}(w, t) e^{j2\pi w(x \cos \theta + y \sin \theta)} w \cdot dw d\theta \quad (5.8)$$

Equation 5.8 can be rewritten as

$$f(x, y, t) = \int_0^{\pi} \left[\int_{-\infty}^{\infty} G_{\theta}(w, t) |w| e^{j2\pi w x} dw \right] d\theta \quad (5.9)$$

The equation inside the bracket in Equation 5.9 represents the filtering operation on each projection, $G_{\theta}(w, t)$. The outer integral represents the back-projection step, hence the name filtered-back projection. [5]

5.2 Computer Simulation

In order to test the filtered-back projection algorithm and the detectability of patterns using only four projections, computer simulations have been performed. A discrete version of the equation 5.9 has been used in conjunction with an appropriate filter. As in the previous experiment, a 1-inch square pit placed in the center of a wafer has been used as a model. Figure 45 describes the template used for the simulation. It is assumed that every point on the wafer except the pit area emits 1 unit of signal in all lateral directions toward detectors. The wafer is assumed to be a 6-inch wafer. Viewing width of each projection is about 2 inches across, which is fairly close to the actual viewing width. Pit area is assumed to be sending out no signals, to simulate the end-point occurrences. Figures 39 through 44 show the simulations performed at various numbers of projection angles.

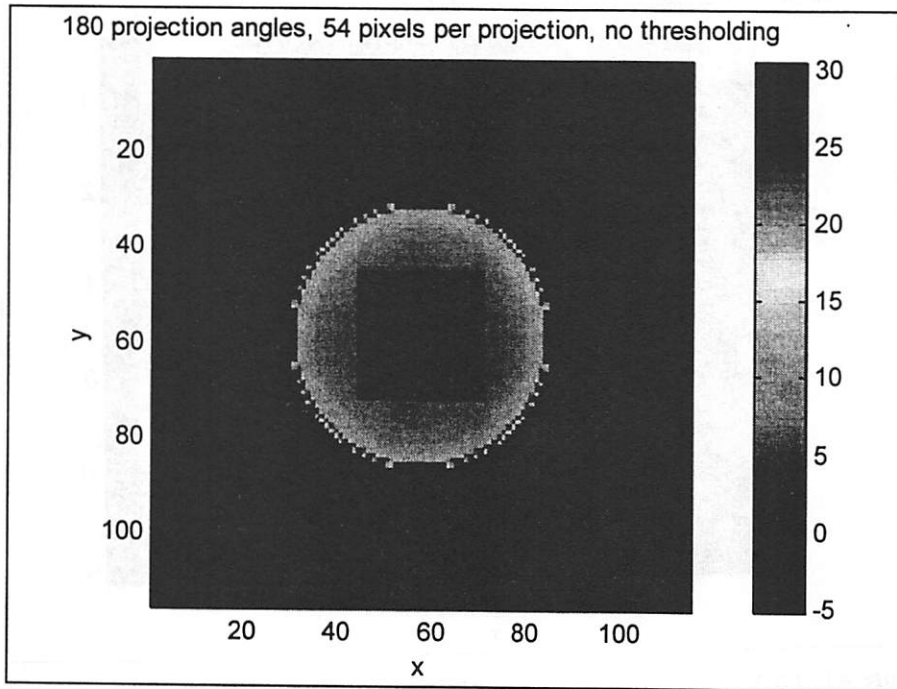


Figure 39. Tomography of the 1-inch pit before thresholding. 180 evenly spaced projection angles are used with 54 pixels spanning 2 inch viewing width.

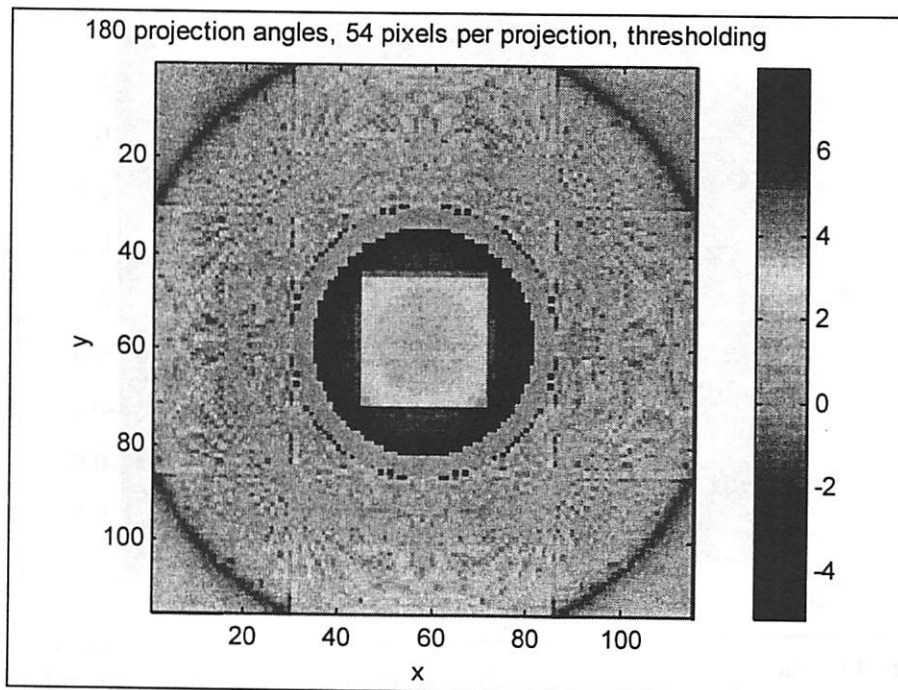


Figure 40. Tomography of the 1-inch pit after thresholding. 180 evenly spaced projection angles are used with 54 pixels spanning 2 inch viewing width.

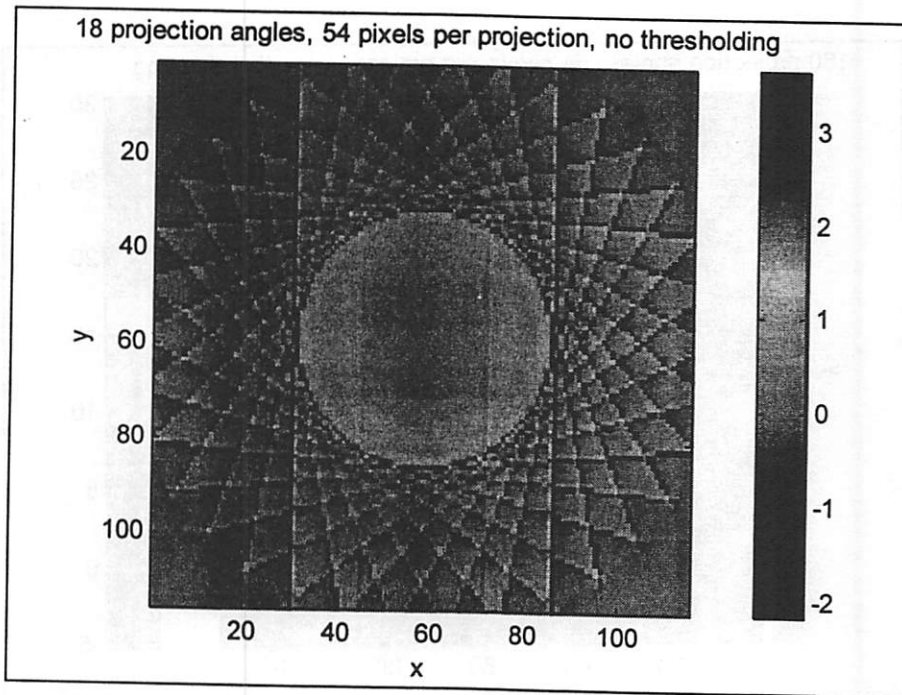


Figure 41. Tomography of the 1-inch pit before thresholding. 18 evenly spaced projection angles are used with 54 pixels spanning 2 inch viewing width.

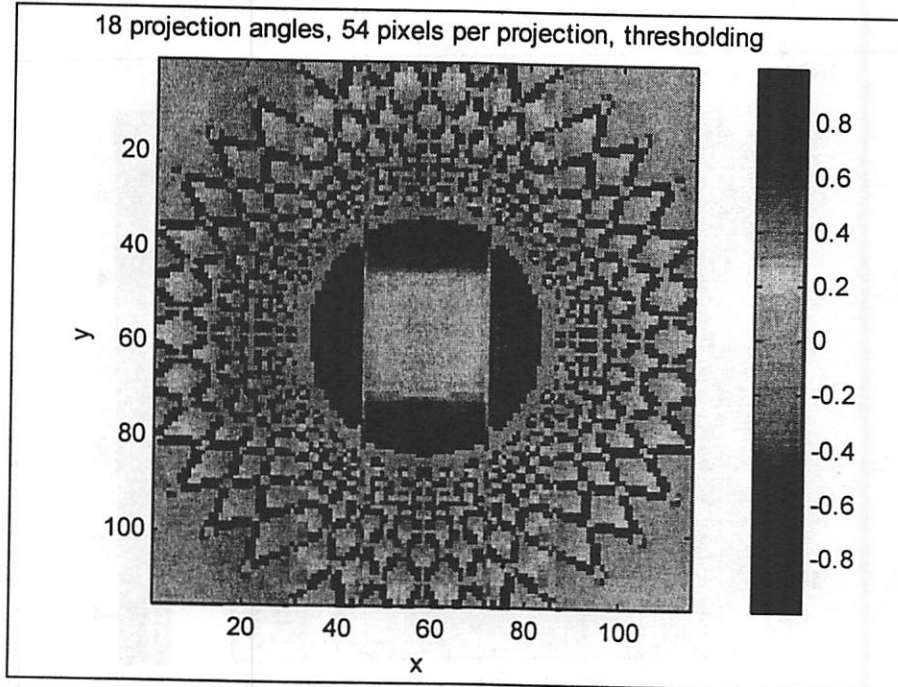


Figure 42. Tomography of the 1-inch pit after thresholding. 18 evenly spaced projection angles are used with 54 pixels spanning 2 inch viewing width.

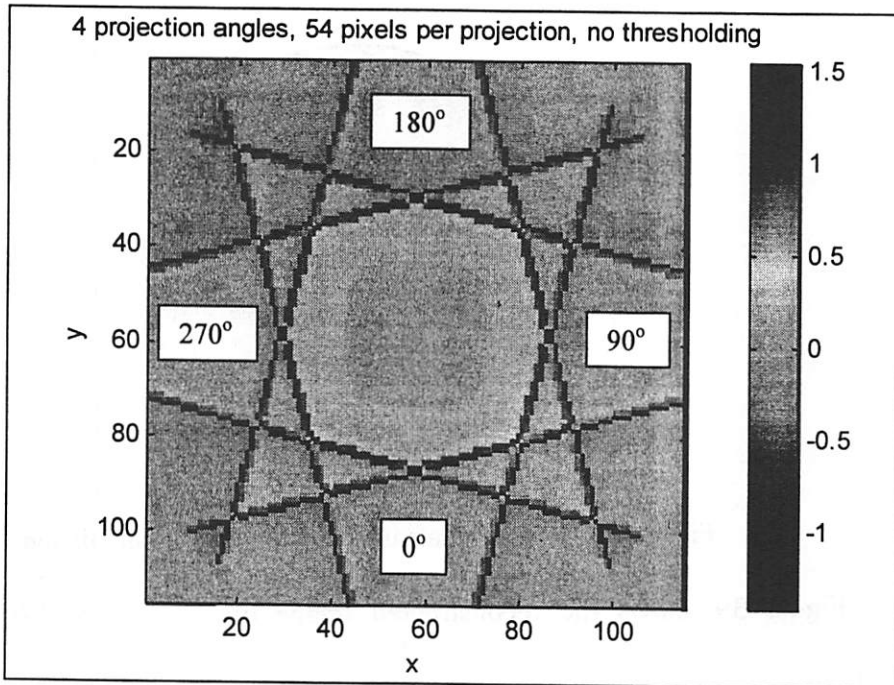


Figure 43. Tomography of the 1-inch pit before thresholding. 4 projection angles, -15° , 15° , 75° , and 105° , are used with 54 pixels spanning 2 inch viewing width.

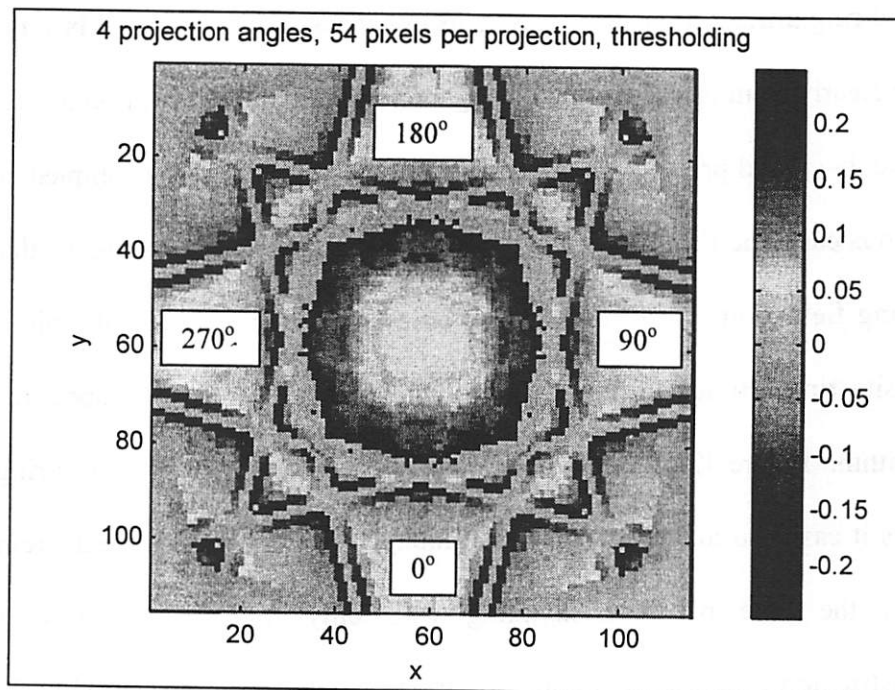


Figure 44. Tomography of the 1-inch pit after thresholding. 4 projection angles, -15° , 15° , 75° , and 105° , are used with 54 pixels spanning 2 inch viewing width.

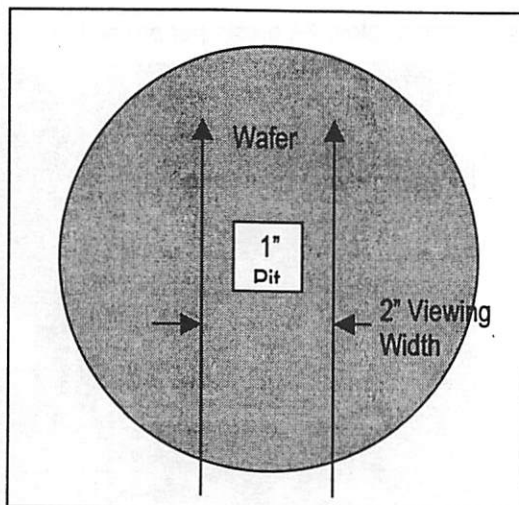


Figure 45. Wafer template used in the computer simulation

Figure 39 shows the reconstructed image obtained from 180 evenly spaced projections. The final image reconstruction is quite smooth and clearly shows the square pit. In Figure 40, a simple thresholding is employed to minimize the reconstruction related ring artifact around the pit. This enhances the contrast and brings out the pattern more clearly from the background. Figure 41 shows the result of reconstruction based on 18 evenly spaced projections. Since this reconstruction is under sampled compared to the previous case, the final image is not as clear as Figure 39. Two streaks that go across the viewing field from top to bottom can be seen on either side of the pit. This and high intensity ring artifact are the results of under-sampling and the specific reconstruction algorithm. Figure 42 employs a thresholding to minimize the effect of ring artifact. This makes it easier to identify the pit even though the two vertical streaks remain. Figure 43 shows the case of under-sampling with only four projection views used. The reconstruction appears to contain a very faint pattern in the middle. Thresholding in Figure 44 enhances the visibility of the pit. Due to under-sampling, the shape of the pit is

not well defined in the reconstruction. Nevertheless, it is possible to identify the rough location of the pit area and approximately estimate the area occupied by the pit.

5.3 Optical Bench Testing

While the wafers were being processed, optical bench tests were performed to obtain more realistic signals for reconstruction. The system described in Figure 46 was set up on an optical bench. The detectors were focused on to the center of the container that held a light-diffusing medium, which was used to crudely simulate the plasma optical condition. First, a 1-inch diameter light source was placed near the center of the container and rotated clockwise. Figure 47 shows the result of the reconstruction. Each frame was taken every 33ms. It turned out that the application of the filtering operation used in the computer simulation did not enhance the detectability of the optical bench signals much if at all. This might be due to the fact that, in the computer simulations, all signals that reached the detector surfaces contributed equal amounts of signal increase regardless of their locations. In reality, each optical fiber strand had non-uniform spatial sensitivity, which resulted in rather significant signal peaks and valleys. Pixels corresponding to the center of the focusing lens received much higher intensity readings compared to the pixels near the edge of the lens. Also, due to the mechanical separation between fibers, there were dead zones where no intensity readings were recorded. Because of the above reasons and the type of filtering used, which amplified high spatial frequency signals, rather sharp edge artifacts persisted in the reconstruction. Therefore, in Figure 47, simple back-projections were performed without any filtering. The rotation and rough location

of the light are shown in the images. Even though much of the signals were diffused, it was possible to distinguish the rough location of the source.

Next, laser beam with a spot diameter of about 3-4mm was rotated near the center of the container. Figure 48 describes the result. As in Figure 47, no spatial filtering was performed in order not to add the undesirable high spatial frequency amplification, which distorted the inter-strand intensity reconstruction. Due to the size of the beam diameter, more localized signals were detected in the images after the reconstruction.

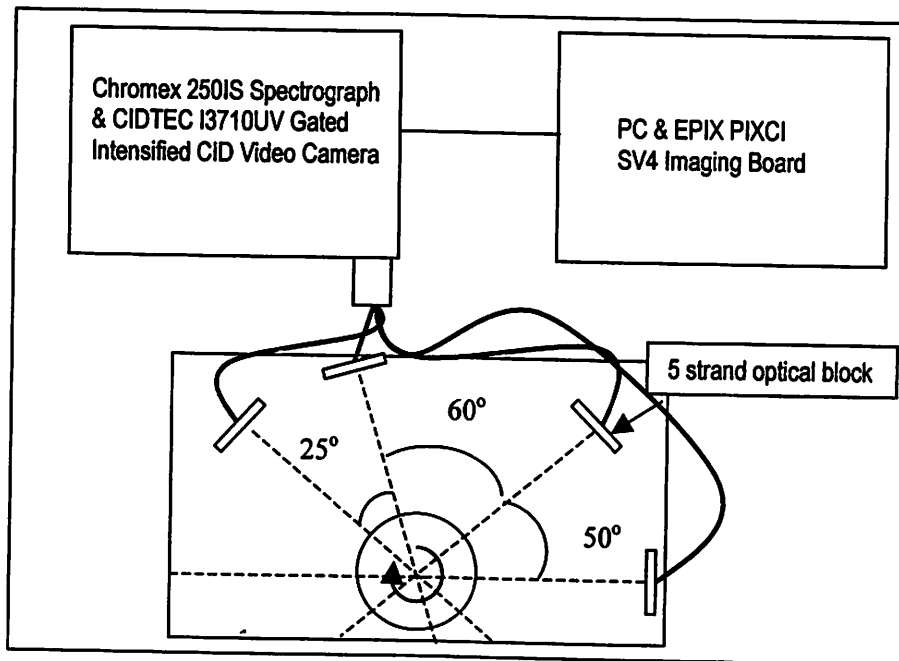


Figure 46. Optical bench test setup

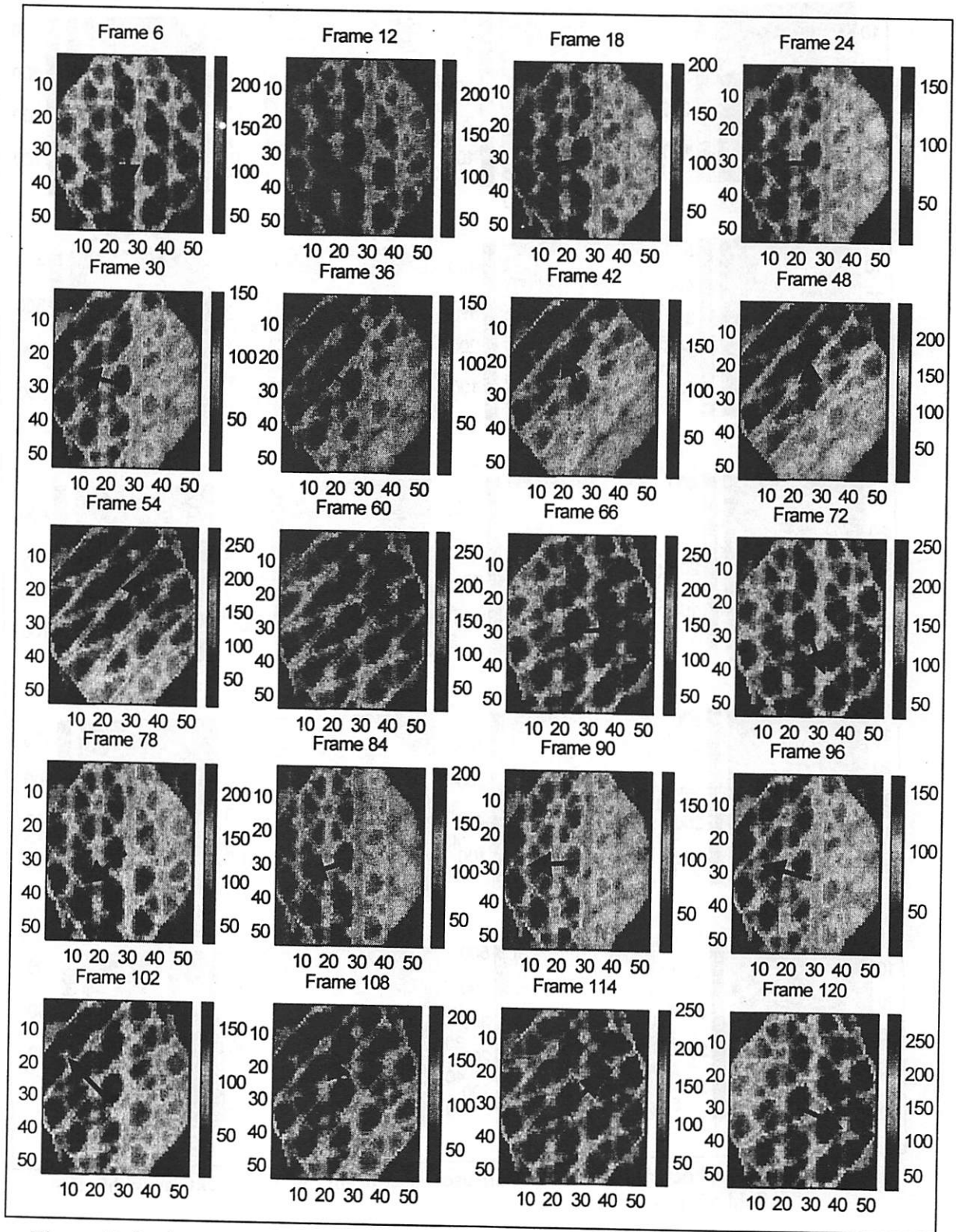


Figure 47. Optical bench simulation of 1-inch diameter flash light rotating clockwise within the field of view.

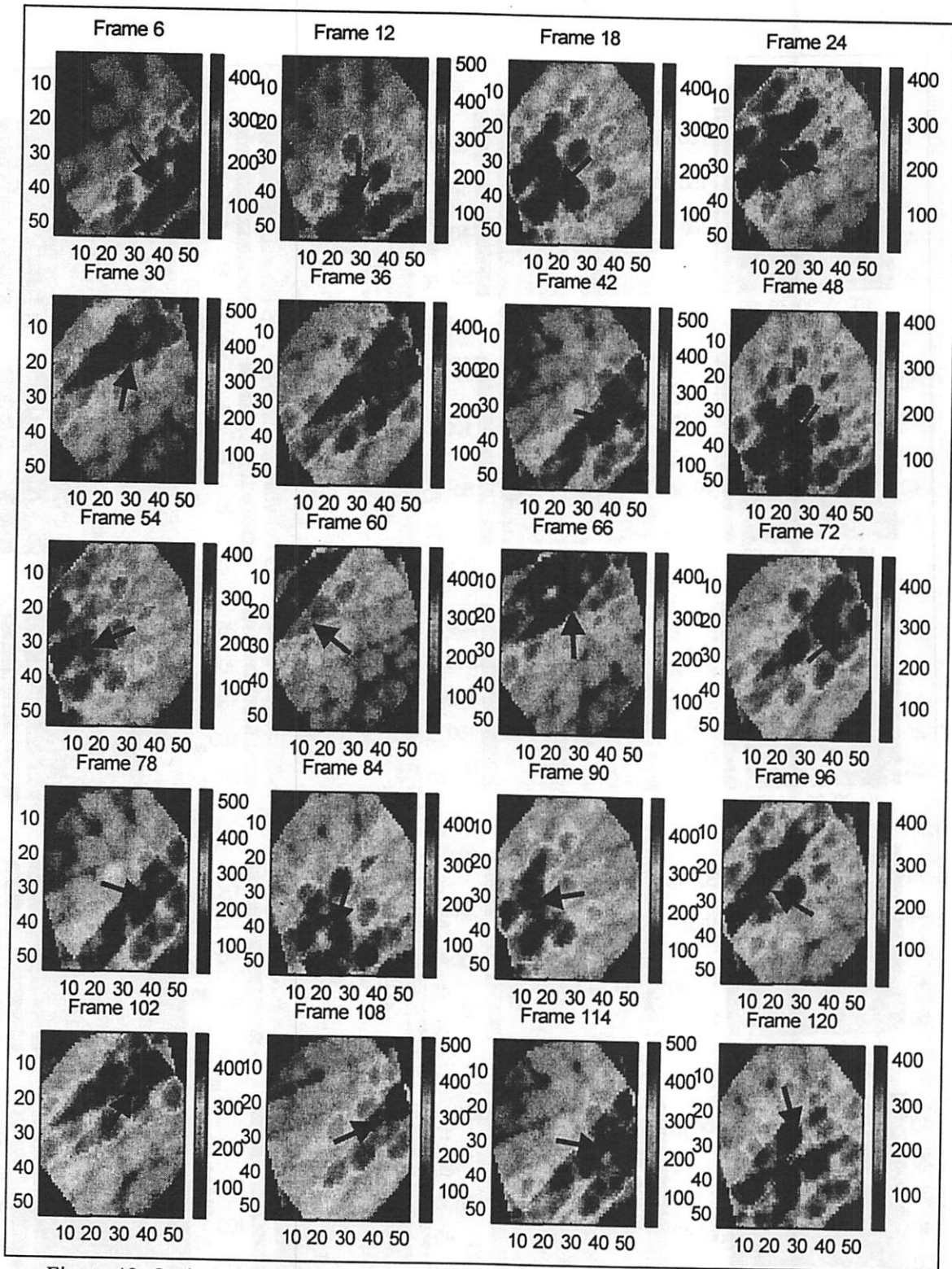


Figure 48. Optical bench simulation of diffused laser beam rotating clockwise within the field of view.

Chapter 6

Tomography Setup

The experimental setup includes 20 individually focused Polymicro Technology FVP 300330370 UV optical fibers. Lenses used to focus each fiber are 014-0086 fused silica plano-convex lenses from OptoSigma. Experiments on Lam TCP 4400 polysilicon plasma etcher in the Microlab at the UC Berkeley has been planned. The plasma etcher has two view-ports available at 90-degree angle as shown in Figure 49 and 50. This arrangement gives a better opportunity for more projection angles around a wafer than Lam TCP 9400, which has one view-port.

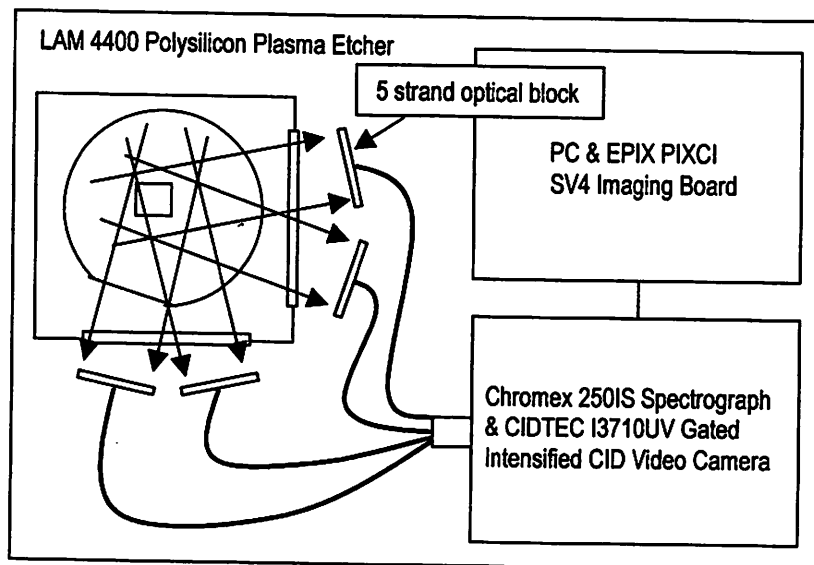


Figure 49. Tomography setup using LAM TCP 4400

Emission gathered by the fibers is transmitted to the entrance slit of a Chromex 250IS imaging spectrograph. Cidtec I3710UV gated intensified CID captures the

resulting two-dimensional emission intensity information (wavelengths and positions across the wafer) at 30 frames per second. The CID delivers 8 bit analog intensity readings. An EPIX PIXCI SV4 imaging board digitizes and stores the analog data.

Each of four fiber blocks in Figure 49 holds five individual fiber strands covering roughly two inches across a wafer. Figure 50 shows the schematics of a fiber block and the fixture used to mount the block to the plasma etcher. All parts with the exception of the fiber blocks have been anodized in order to minimize reflections off the fixture. The Chromex plug head that goes into the spectrograph is similar to that in Figure 8, with 20 fibers spread out to fit the height of the CID chip. Figure 51 shows the picture actual setup prior to the experiment

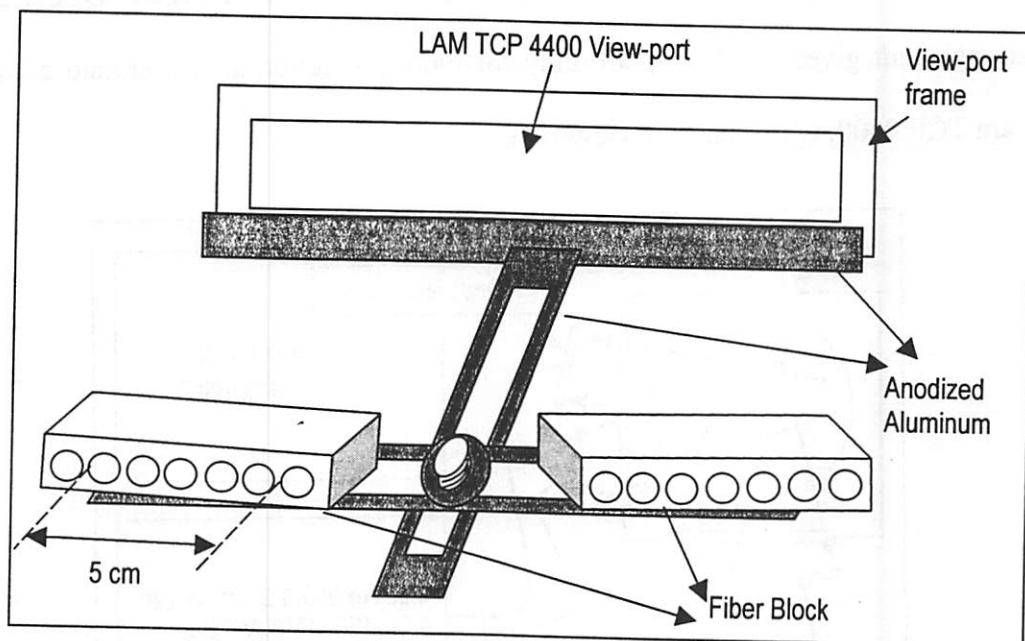


Figure 50. Fiber block and view-port fixture schematics

As for the test wafers, only two types have been prepared. The LAM 4400 at the Microlab uses the same Cl_2 based chemistry as the LAM 9400. However, the etching rate is only about 80 % of LAM 9400 etching rate, which results in lower SiCl_2 and other

etching byproducts flux during the main etching. Therefore, 1cm pits have not been produced due to its weak signal levels. Also, due to optical obstructions caused by wafer support bars in front of both view-ports, only 2nd quadrant pitted wafers have been produced. Pitted wafers contain 50 % open areas as shown in Figure 52. Also, in order to measure the emission transient signals, wafers with 50 % open areas but without pits are processed.

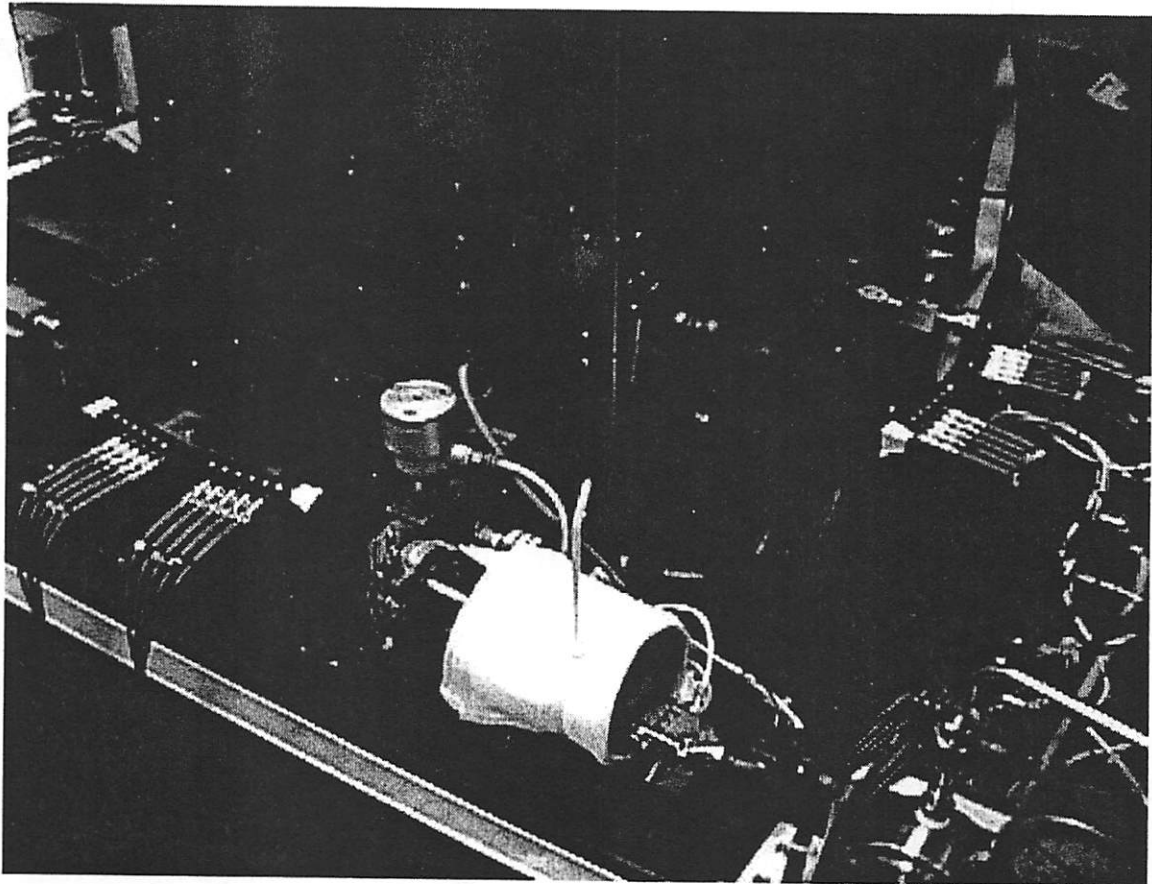


Figure 51. Optical emission tomography setup on LAM TCP 4400

The wafer processing steps are as follows. First, 300 Å of SiO₂ layer is thermally grown on all 4 wafers. Then, roughly 6000 Å of polysilicon layer is deposited using low-pressure chemical vapor deposition (LPCVD) on all 4 wafers. Finally, a 1:1 contact mask with a 1-inch² opening is used to pattern two wafers. These wafers are pre-thinned

using Lam TCP 4400. The pit area polysilicon thickness is reduced down to about 1000-1100 Å. A second mask with 50% open areas is used to pattern all 4 wafers.

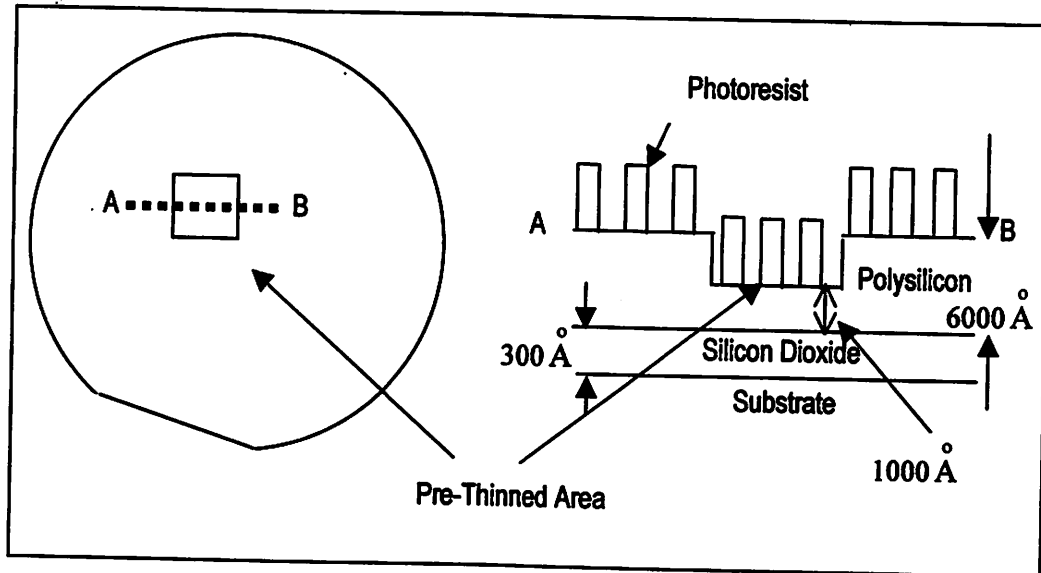


Figure 52. A 2nd quadrant pitted wafer and its cross section.

Chapter 7

Results and Analysis II

Figures 53 through 60 show the normalized, reconstructed images from the four-wafer run. Figures 53 & 54 and 55 & 56 contain signals gathered before and after end-points from the first and second baseline wafers respectively. Figures 57 & 58 and 59 & 60 contain signals gathered before and after end-points from the first and second pitted wafers respectively. The figures demonstrate that the occurrences of end-points are detected by the setup. Also, we can see the distinction between the baseline wafer post end-point signals and pitted wafer post end-point signals. However, due to the narrowness of the gap between the rings surrounding the electrodes and the semi-circular holes on them, which have contributed much higher signal intensity at certain positions, it is not possible to tell the spatially resolved occurrences of the end-points. The presence of the holes on the surrounding ring is more crucial to our setup since the setup can only deliver 8-bit intensity resolution. Since the signals from certain portions of the wafer get much more amplification, the signal range reserved for other lower intensity locations is much reduced, resulting in poor or no detection. Figure 61 shows the raw, reconstructed image before the end-point of a pitted wafer. As the figure shows, the circled location has the intensity that is more than twice higher than the surrounding regions. This was not a problem in the previous 1-D SROES experiment since the beam spot size was much smaller and fibers were physically very close together.

There are several modifications that can be made in order to improve the detectability of the spatially resolved end-points. First, rings without holes can replace the pair of rings around the electrodes, assuming this does not change the etching significantly. Second, wavelength information can be traded for better dynamic range. This can be done by using a one-dimensional imaging chip in conjunction with a wavelength filter. Third, a better chamber geometry can be used to improve the viewing angle and the number of projections. Figure 62 describes a potential chamber configuration that is ideal for a tomography.

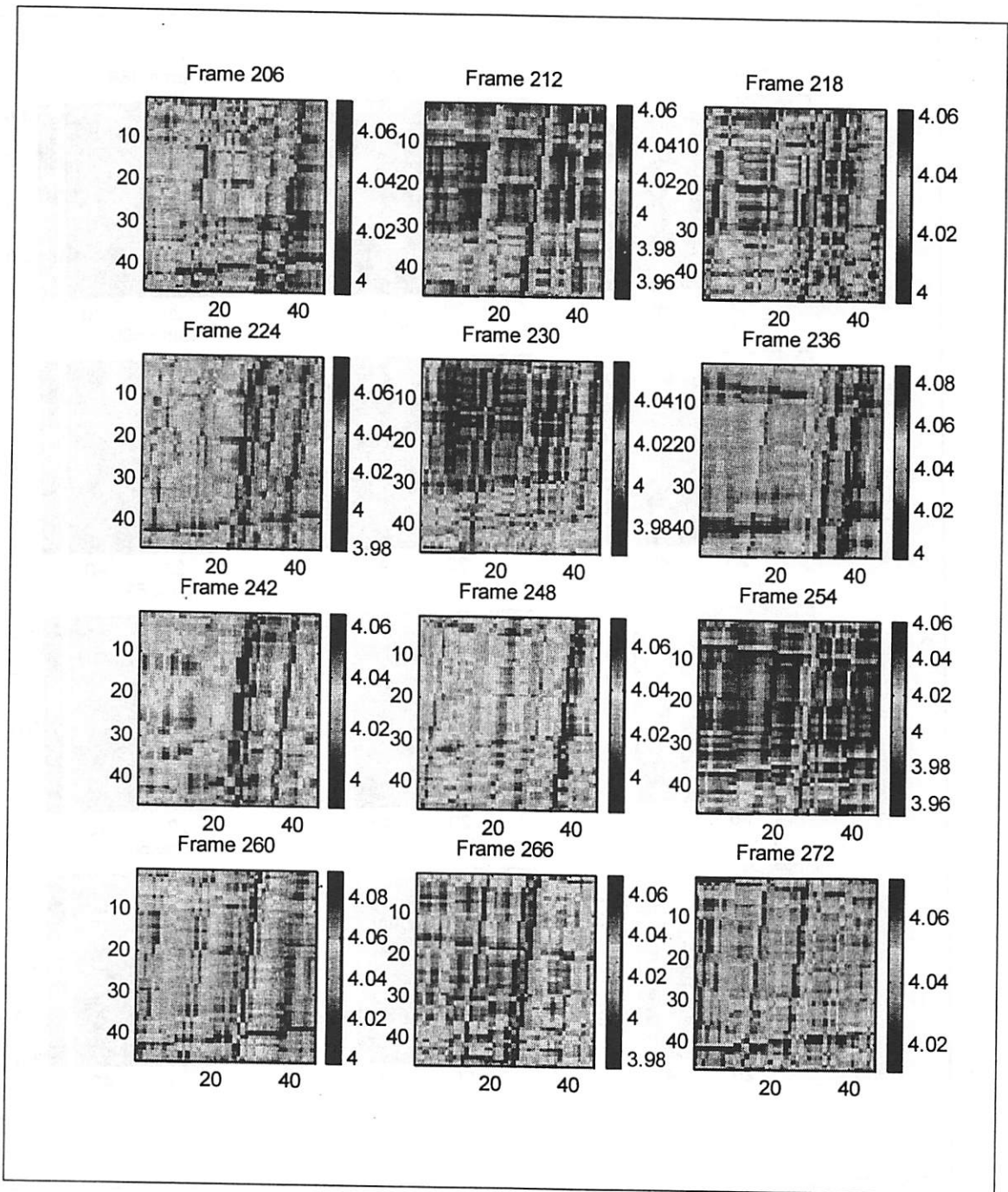


Figure 53. Spatially normalized 1st baseline wafer signal before the end-point occurrences. x and y axes represent spatial coordinates covering roughly 1.5 in. on each side.

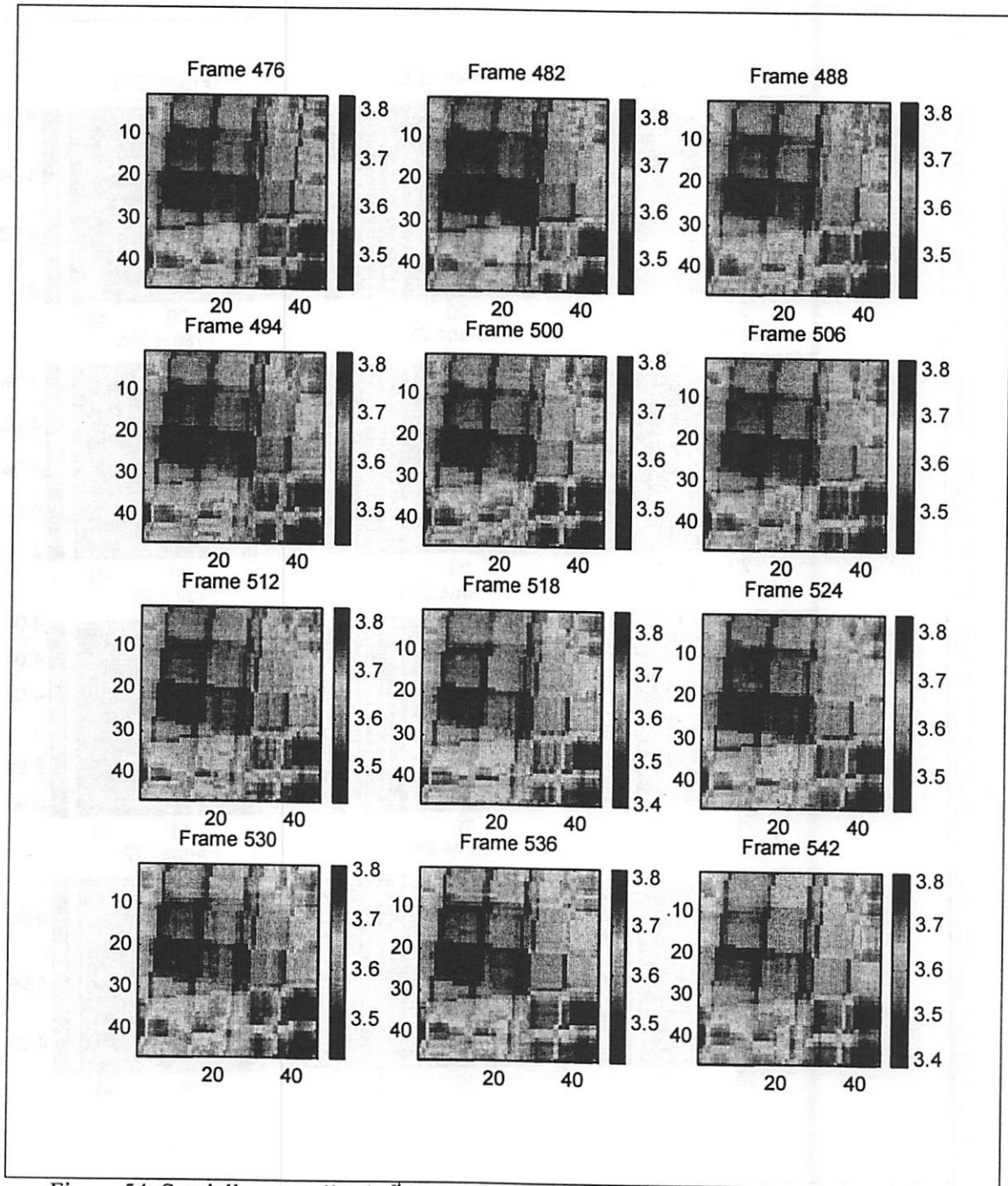


Figure 54. Spatially normalized 1st baseline wafer signal after the end-point occurrences. x and y axes represent spatial coordinates covering roughly 1.5 in. on each side.

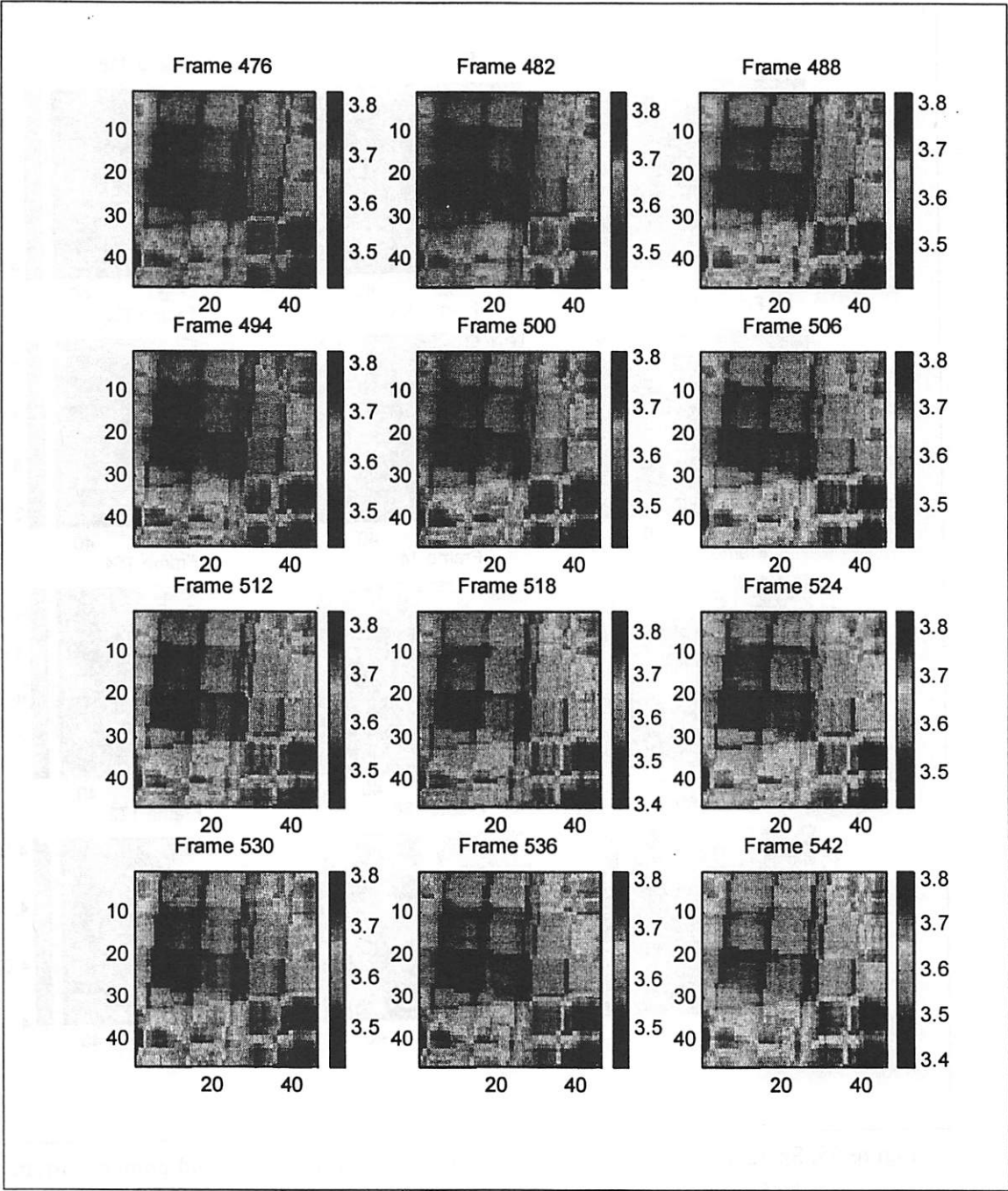


Figure 54. Spatially normalized 1st baseline wafer signal after the end-point occurrences. x and y axes represent spatial coordinates covering roughly 1.5 in. on each side.

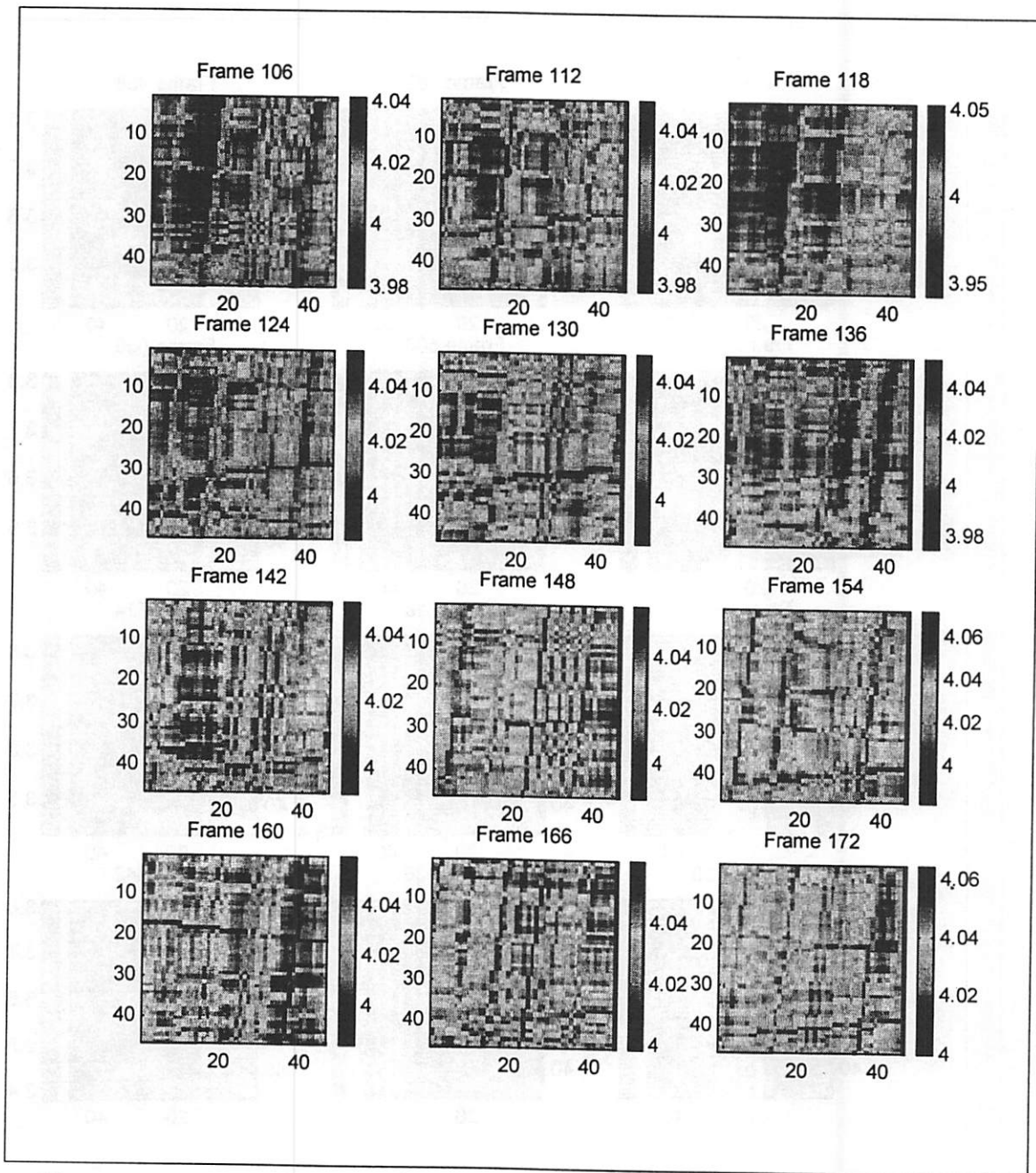


Figure 55. Spatially normalized 2nd baseline wafer signal before the end-point occurrences. x and y axes represent spatial coordinates covering roughly 1.5 in. on each side.

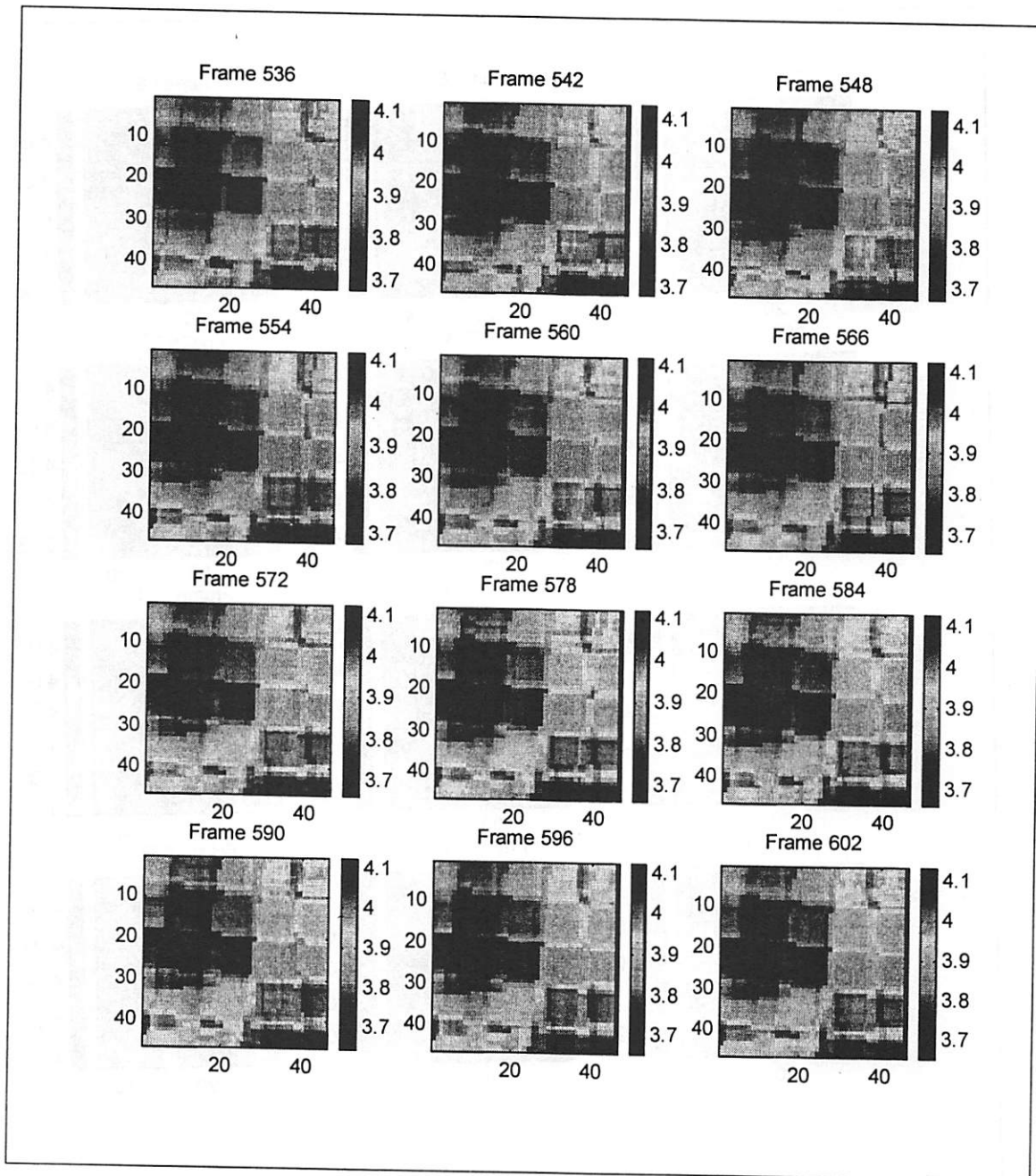


Figure 56. Spatially normalized 2nd baseline wafer signal after the end-point occurrences. x and y axes represent spatial coordinates covering roughly 1.5 in. on each side.

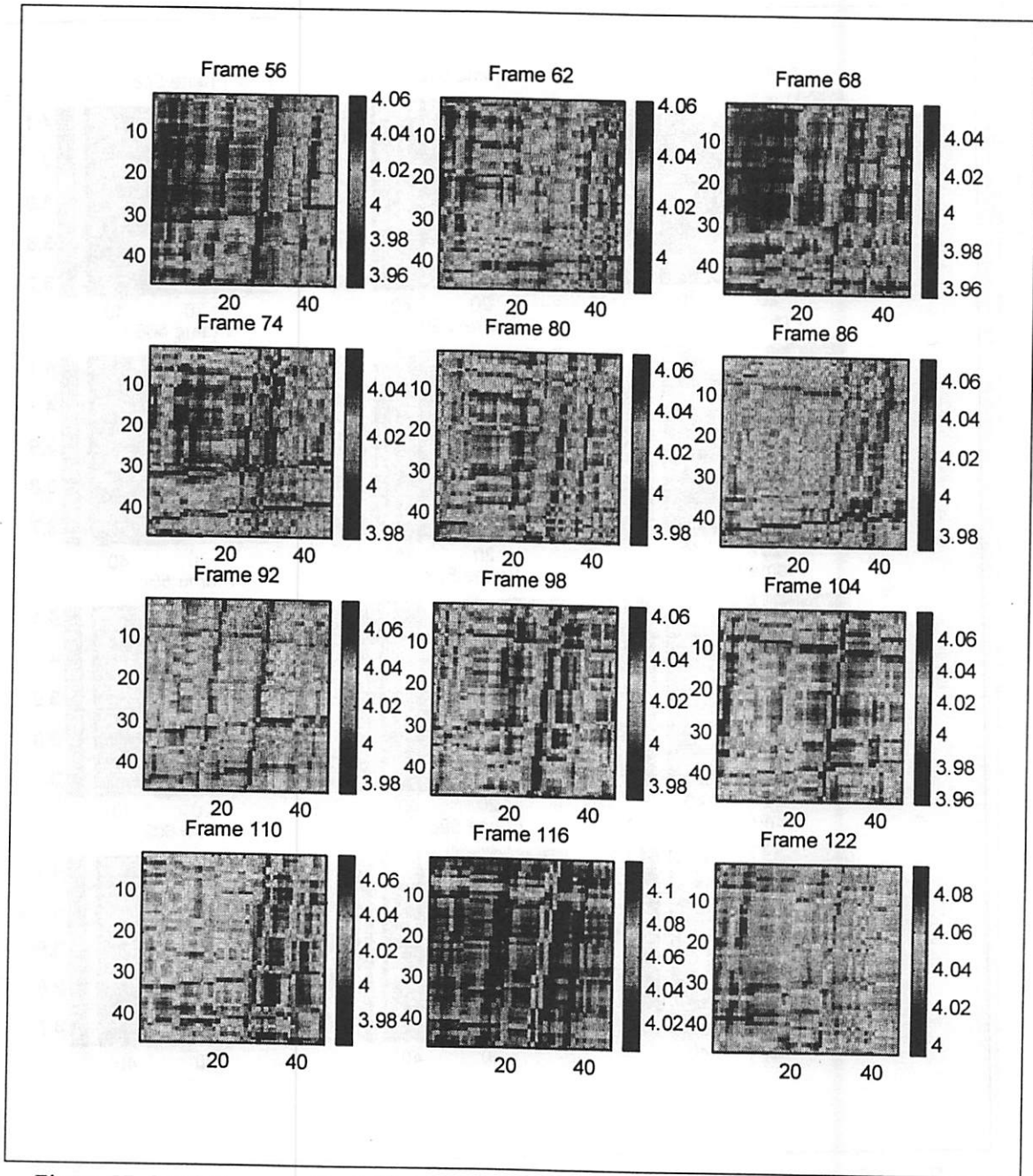


Figure 57. Spatially normalized 1st pitted wafer signal before the pit end-point occurrences. x and y axes represent spatial coordinates covering roughly 1.5 in. on each side.

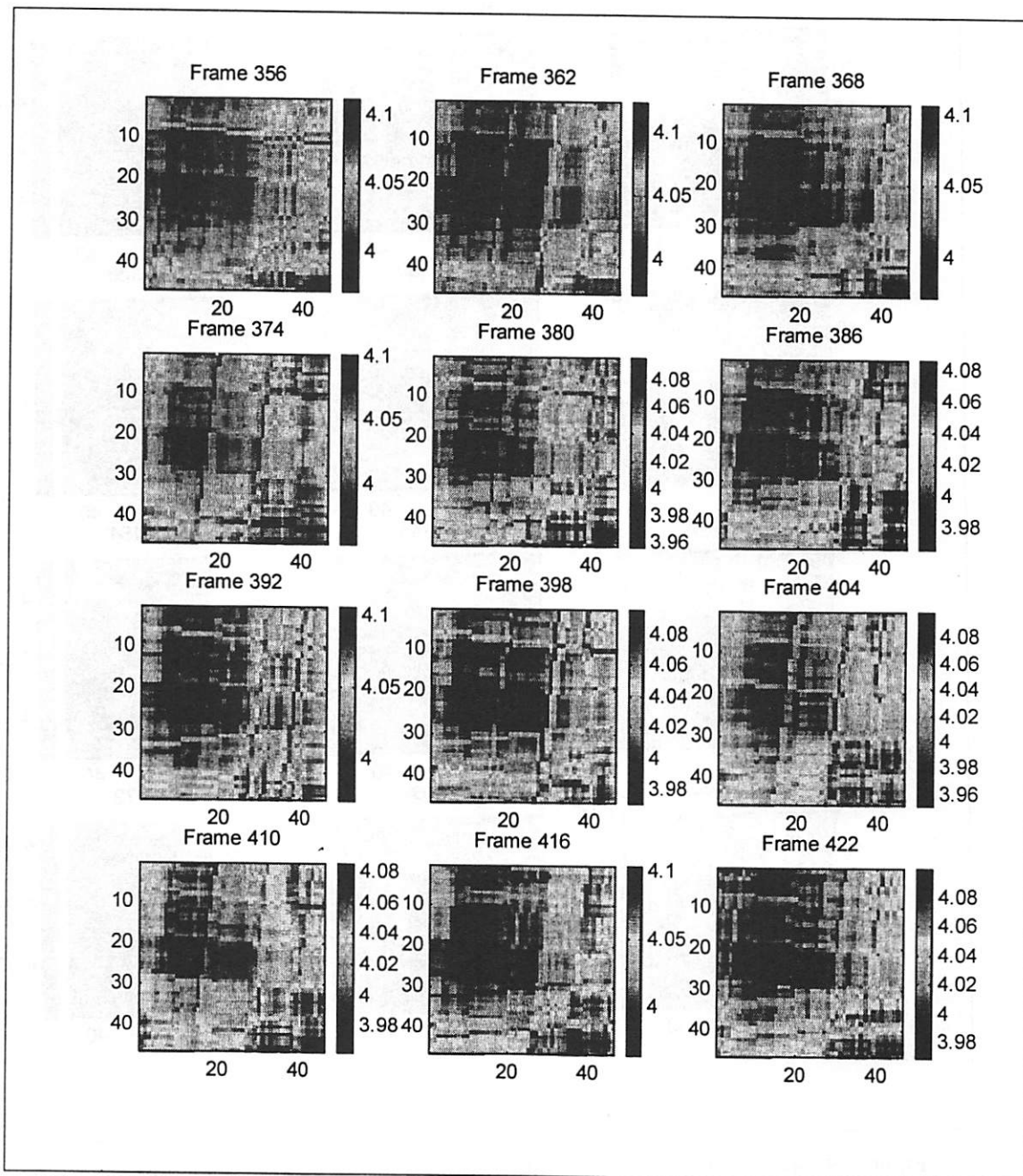


Figure 58. Spatially normalized 1st pitted wafer signal after the pit end-point occurrences. x and y axes represent spatial coordinates covering roughly 1.5 in. on each side.

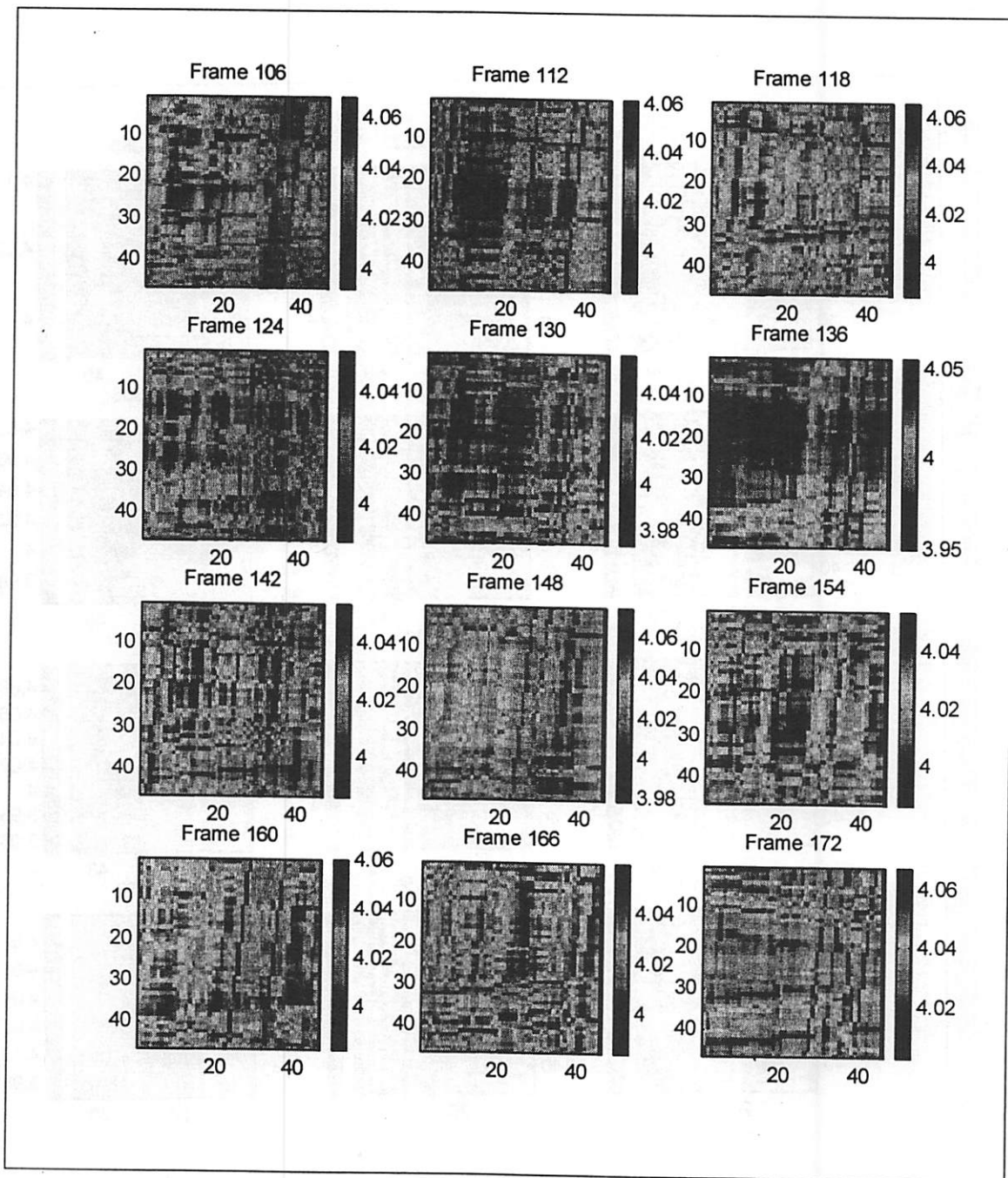


Figure 59. Spatially normalized 2nd pitted wafer signal before the pit end-point occurrences. x and y axes represent spatial coordinates covering roughly 1.5 in. on each side.

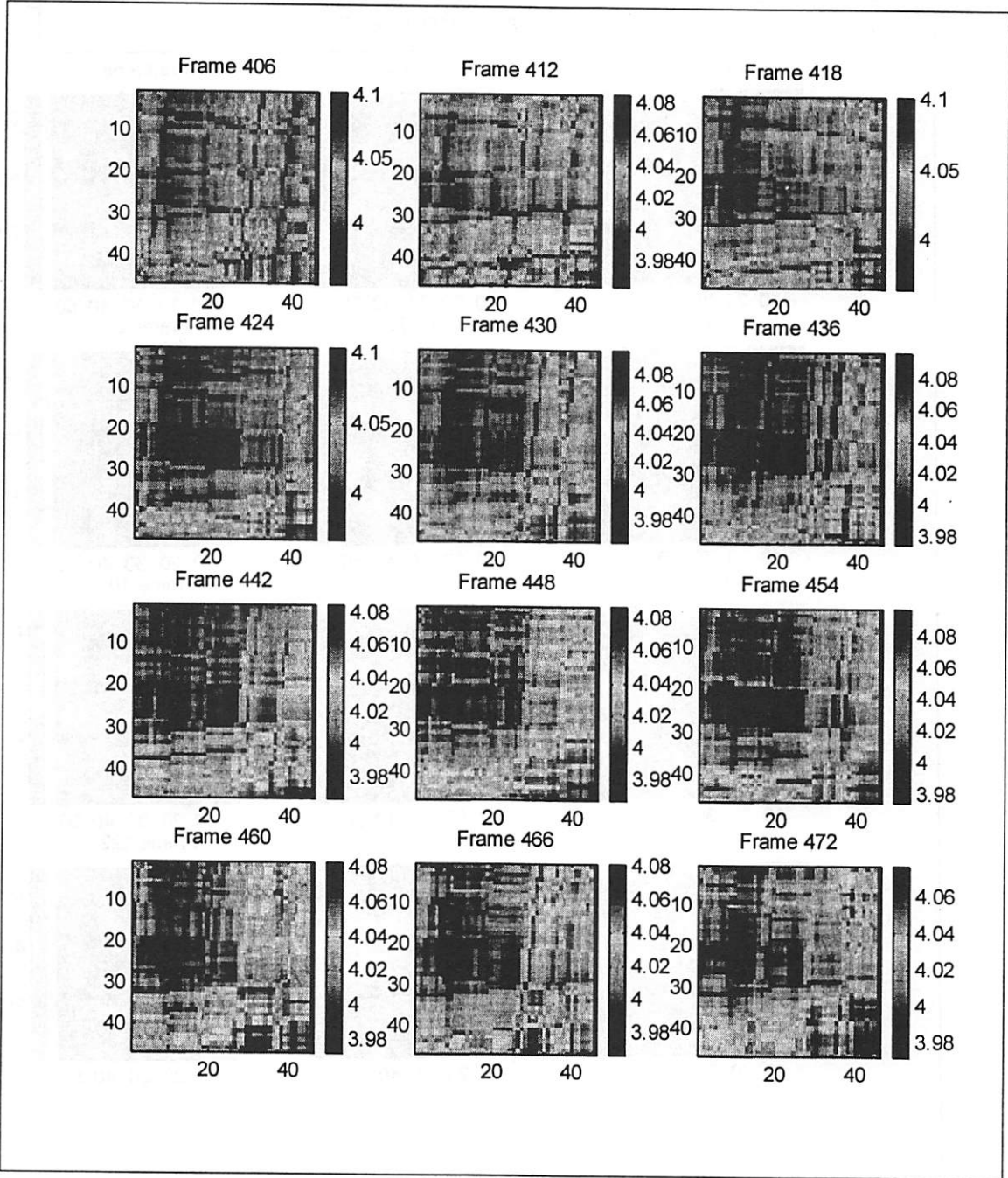


Figure 60. Spatially normalized 2nd pitted wafer signal after the pit end-point occurrences. x and y axes represent spatial coordinates covering roughly 1.5 in. on each side.

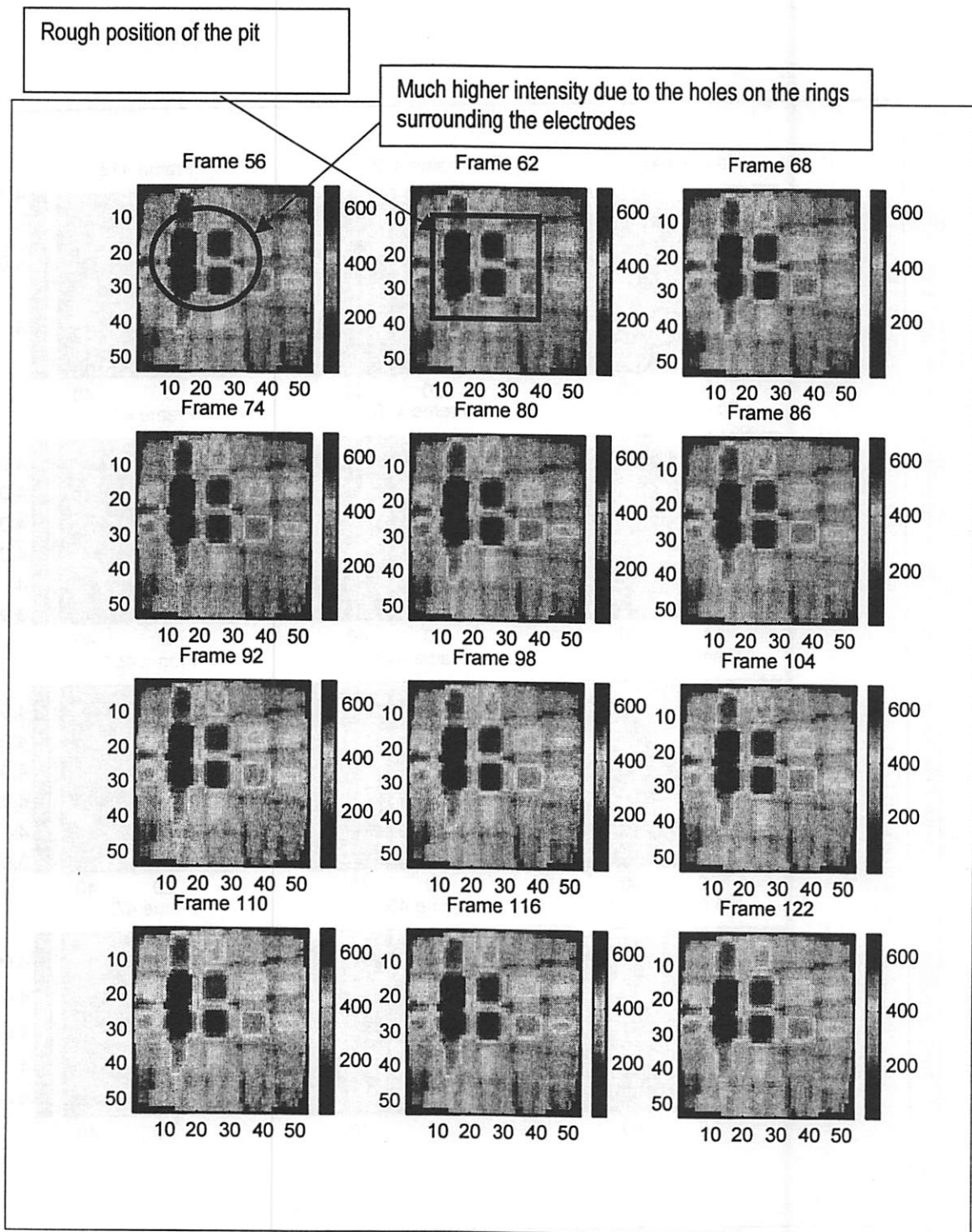


Figure 61. Raw 1st pitted wafer signal before the pit end-point occurrences. x and y axes represent spatial coordinates covering roughly 1.75 in. on each side. The data is used to produce Figure 57.

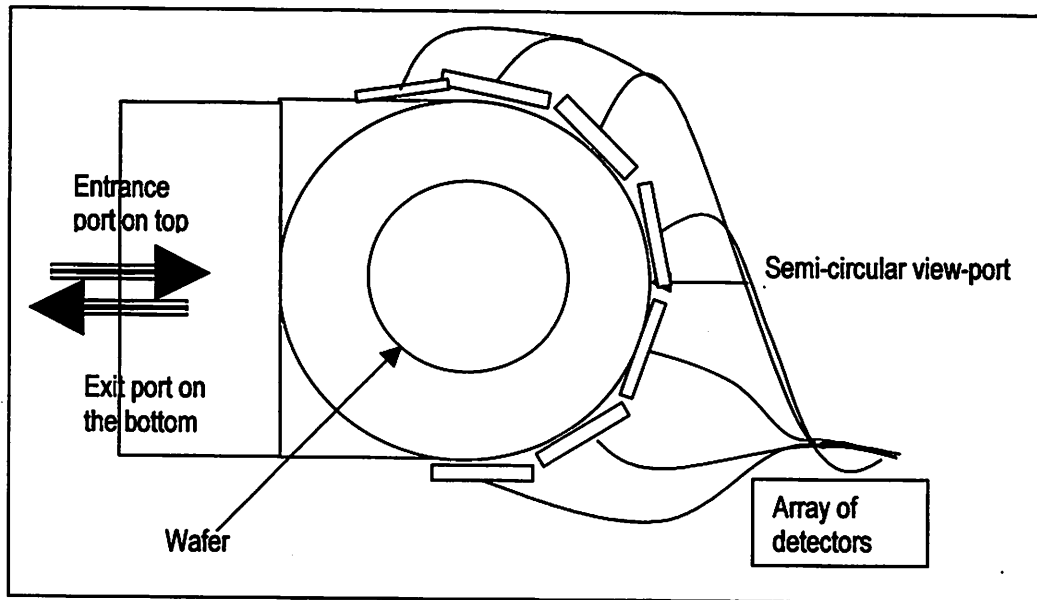


Figure 62. An ideal chamber configuration for end-point tomography

References

- [1] M. J. Buie et al, "Abel's Inversion Applied to Experimental Spectroscopic Data with Off Axis Peaks", *Journal of Quantitative Spectroscopy and Radiation Transfer*, vol. 55, no. 2, pp. 231-243, 1996.
- [2] S. Shannon et al, "A Spatially Resolved Optical Emission Sensor for Plasma Etch Monitoring", *Applied Physics Letter*, vol. 71, pp. 1467-1468, 1997.
- [3] Roawen Chen, "Chapter 6: Scanning Spatially Resolved OES", *OES-Based Sensing for Plasma Processing in IC manufacturing*, Ph.D. Thesis, Dec. 1997.
- [4] Anil K. Jain, *Fundamentals of Digital Image Processing*, Prentice Hall, Inc., Englewood Cliffs, New Jersey, 1989.
- [5] Avinash C. Kak and Slaney, *Principles of Computerized Tomographic Imaging*, The Institute of Electrical and Electronics Engineers, Inc., New York, New York, 1988.
- [6] www.ctlab.geo.utexas.edu
- [7] www.eecs.berkeley.edu/~budinger